Title: Building Change Detection in Multitemporal Very High Resolution SAR Images

This paper appears in: IEEE Transactions on Geoscience and Remote Sensing

Date of Publication: 05 November 2014

Author(s): C. Marin, F. Bovolo, L. Bruzzone

Volume: 53, Issue: 5

Page(s): 2664 - 2682

Product Type: Journals & Magazines

DOI: 10.1109/TGRS.2014.2363548

URL: http://dx.doi.org/10.1109/TGRS.2014.2363548

Building Change Detection in Multitemporal Very High Resolution SAR Images

Carlo Marin, *Student Member, IEEE,* Francesca Bovolo, *Senior Member, IEEE,*
and Lorenzo Bruzzone, *Fellow, IEEE*

Abstract

The increasing availability of very high resolution (VHR) images regularly acquired over urban areas opens new attractive opportunities for monitoring human settlements at the level of individual buildings. This paper presents a novel approach to building change detection in multitemporal VHR Synthetic Aperture Radar (SAR) images. The proposed approach is based on two concepts: i) the extraction of information on changes associated with increase and decrease of backscattering at the optimal building scale; and ii) the exploitation of the expected backscattering properties of buildings to detect either new or fully demolished buildings. Each detected change is associated with a grade of reliability. The approach is validated on a) COSMO-SkyMed multitemporal spotlight images acquired in 2009 on the city of L'Aquila (Italy) before and after the earthquake that hit the region, and b) TerraSAR-X multitemporal spotlight images acquired on the urban area of the city of Trento (Italy). Results demonstrate that the proposed approach allows an accurate identification of new and demolished buildings while presents a low false alarm rate and a high reliability.

Index Terms

Multitemporal images, building change detection, very high geometrical resolution images, synthetic aperture radar, change detection, remote sensing.

I. Introduction

Monitoring of urban areas is of great importance for several applications such as urban planning, cadastral map updating, environmental monitoring, disaster assessment and so on. The uncensored synoptic view and the repeat-pass nature of satellites render them an ideal platform from where acquiring information about human settlements. Nonetheless, the huge amount of data acquired from the satellite sensors requires the development of automatic algorithms that can process the data and extract the desired information without any manual processing or ground truth information. In the last decades a new generation of satellite sensors has been operated, which can regularly

C. Marin, and L. Bruzzone are with the Department of Information Engineering and Computer Science, University of Trento Via Sommarive, 5 I-38123, Povo, Trento, Italy, (e-mail: lorenzo.bruzzone@ing.unitn.it). F. Bovolo is with Fondazione Bruno Kessler (FBK) Via Sommarive, 18 I-38123, Povo, Trento, Italy (e-mail: bovolo@fbk.eu)

Manuscript received Month Day, Year; revised Month Day, Year.

acquire very high geometrical resolution (VHR) images i.e., images having a resolution of a meter or less. The increasing availability of such data allows the analysis of urban areas at a detail level never reached before resulting in the possibility of detecting buildings individually. In this context, several automatic techniques for the study of urban areas have been developed by exploiting both active Synthetic Aperture Radar (SAR) and passive sensors [1]–[5]. Between these two technologies, the use of SAR systems for addressing the problem of monitoring urban area changes is very attractive from an operational point of view since, different from optical sensors, SAR is independent from the sun illumination and it is relatively insensitive to atmospheric weather conditions. This makes it possible to plan either the acquisition of data in advance (e.g., according to end-user requirements without unpredictable intervention of atmospheric effects) and to ensure data availability during crisis events (e.g., floods, earthquakes). Nowadays several SAR missions are operating that can acquire regularly VHR SAR images. Among them we recall TerraSAR-X, Tandem-X and the COSMO-SkyMed constellation. Data acquired from these missions can be exploited to detect changes in urban areas at the level of each single building. Nevertheless, the combination of high resolution and multitemporal analysis leads to some challenging issues that should be addressed.

VHR SAR images are more heterogeneous than high or medium resolution data [6], [7]. Objects that are considered homogeneous from a semantic point of view (e.g., buildings) show a signature that is inhomogeneous at high spatial resolution because of the scattering contributions from sub-objects (e.g., facade and roof in a building). Furthermore, on the one hand the side-looking illumination required by SAR systems leads to phenomena such as layover, shadow and multi-path signals [8], [9], which are very pronounced in urban areas. On the other hand, the appearance of a ground object depends on radar system parameters (i.e., wavelength, polarization, pulse length, incidence angle, look direction, etc.), surface feature properties (e.g., dielectric constant) and environmental variables (e.g., ground water content) [10]. On top of these aspects, SAR images are corrupted by speckle noise.

All these factors, propagated to the multitemporal analysis, make the problem of the detection of changes complex. Due to the high resolution a large set of possible changes with different semantic meaning and scale are detectable in multitemporal VHR SAR images. In general, each change may be associated with the cause of the change itself [11] and may present an extension that varies from the single pixel to a relevant portion of the entire scene. For instance it is possible to distinguish among changes due to the anthropogenic activity, the phenological evolution of the vegetation and the natural disasters. Depending on the application, some of these may be of interest to the end-users, whereas others may not [12]. In addition, external factors, such as different content of water on the ground due to different weather conditions may affect the local backscattering behaviors at two dates also in absence of any other change. Therefore, the same object may show different value of backscattering even though it is not affected by a relevant change. This invalidates the assumption that two SAR images acquired on the same geographical area at different times are similar to each other except for the presence of changes occurred on the ground, which is often considered for high- and medium-resolution SAR images. Thus the use of standard pixel based change detection (CD) techniques is not applicable as they would be affected by a large amount of false alarms. Given the complexity of the problem, also standard context-based techniques based on a local neighborhood analysis would fail to solve the problem since they are not able to properly take into account the high geometrical detail of VHR

data. To achieve CD in VHR SAR images the comparison between the multitemporal images should be performed at a higher conceptual level that models the source of change from the prospective of interactions with the incidence electromagnetic wave.

Numerous studies have been recently presented in the literature that deal with the problems of recognition of changes in urban areas using VHR SAR images [13]–[25]. In detail, [13]–[22] are focused on the detection of earthquake damages, [23] is focused on the building databases updating, and [24] addresses the detection of changes due to the urban evolution. The strategies that are exploited in these papers include post-event supervised analysis [15], [17], [20]–[22], joint use of optical and SAR data [14], [16], joint use of LiDAR and SAR data [24], unsupervised detection of damages at the level of aggregated blocks [13], [18] or GIS polygons [19]. Despite the great interest, the only work that addresses the problem of building change detection using multitemporal VHR SAR data in an unsupervised way is presented in [25]. In detail, the authors present an approach to the detection of damaged structures in urban areas from VHR SAR images, which is based on the multitemporal detection of double-bounce line generated by the multiple backscattering between the wall of the building and the ground. If a double-bounce line appears (disappears) between two acquisitions a new (destroyed) building is recognized. The method uses only one of the salient feature used for detecting a building. This partial modeling of the source of change may generate a relevant number of missed alarms. Furthermore, the double-bounce line of a building alone is not a reliable feature for the identification of buildings because in several cases it may be not visible [26].

In this paper, which generalizes and extends the work presented in [27] and [28], we propose a novel approach to building change detection in VHR SAR images that: i) is unsupervised; ii) extends the studies on the backscattering properties of buildings presented in the literature for single date images [29]–[35] to bi-temporal images; iii) takes advantage of the multitemporal correlation between images; iv) considers the intrinsic multiscale nature of objects present in VHR images; and v) is flexible. In greater detail, the approach is based on two concepts: i) the extraction of information on changes associated with increase and decrease of backscattering at the optimal building scale; and ii) the exploitation of the expected backscattering properties of buildings to detect new and fully demolished buildings with their grade of reliability. The effectiveness of the proposed approach is demonstrated in experiments carried out on two data-sets: the former is acquired by COSMO-SkyMed satellites over L'Aquila, Italy, which was heavily damaged during the 2009 earthquake. The latter is acquired by TerraSAR-X and Tandem-X over the city of Trento, Italy and it represents the urban evolution of the city from 2011 to 2013.

The paper is organized into five sections. Section II presents and reviews the fundamentals of the backscattering mechanism of buildings in monotemporal images. Moreover it proposes an analysis of this mechanism for bi-temporal SAR images. This introduces the concept used in the proposed approach. The proposed approach to building change detection is described in Section III. Section IV presents the data set and show the experimental results. Section V draws the conclusions of the work. The mathematical notation used in the paper is listed in the appendix.

II. Fundamentals on the Building Backscattering Mechanism

In this section we analyze the backscattering mechanisms with respect to the variation of the acquisition geometry when isolated buildings with rectangular layout are sensed by VHR SAR (Section II-A). This analysis is used to interpret multitemporal VHR SAR images in order to study and model the effects associated with new/demolished building (Section II-B). This study gives the base for the development of the proposed approach.

A. Building Backscattering Mechanisms in Single Detected VHR SAR Images

SAR is an active system that measures the backscatter of a transmitted signal in the microwaves portion of the spectrum. The backscattering value is mainly determined by the geometry of acquisition, the dielectric and geometric properties of the target, and the transmission configuration of the antenna [10], [37]. In the literature several works have been presented that analyzed the scattering mechanism for different building models in order to derive their appearance in SAR images [16], [31], [38]. These analyses make use of the geometrical optics (ray theory) approximation in order to model the electromagnetic scattering. This has the power to be intuitive and geometrically accurate even though the electromagnetic interactions and the transmission configurations of the antenna are not taken into account. In geometrical optics the wave propagation is described by rays, which are modeled as lines perpendicular to the wavefronts, that may be reflected, absorbed or split at the interface between two media. By knowing the geometry of acquisition of the SAR system and by exploiting trigonometric functions it is possible to simulate the appearance of a building in VHR SAR images [16], [31], [38].

Let us consider an isolated flat-roof building with dimensions $w_1 \times w_2 \times h$ illuminated by a SAR sensor that is moving along the azimuth direction and is illuminating the building from the left (Fig. 1a). Let us consider a building model that does not take into account the building features such as windows, eaves, ridges, railings and so on. This is equivalent to analyze the image at the scale level comparable with the building, and it allows us to derive the appearance of a building without losing generality. The acquisition geometry of a SAR system (Fig. 1a) is characterized by two parameters: the incidence angle θ (i.e., the angle defined by the incident radar beam and the normal to the intercepting surface) that is generally included between 20° to 55°, and the aspect angle $0^\circ \leq \phi < 90^\circ$ (i.e., the angle between the azimuth direction and the orientation of an object in the horizontal plane). For the sake of argument, let us first assume that the SAR sensor illuminates the section A-A (light blue area in Fig. 1a) of the building from a fixed position in the azimuth. Fig. 1b shows in a qualitative way the amplitude of the backscattering projected in ground range and slant range of A-A. Following [16] the main contributions that can be identified are: the return a from the ground, the double bounce effect b caused by the dihedral reflector formed by the building wall and the ground, the backscattering c from the front wall, the returns d from the building roof and the shadow area e (see Fig. 1b). As one can observe the contributions from the ground, the wall and the roof are summed up into an area in front of the building ($a + c + d$), which appears brighter than each of these contributions taken singularly because of their superposition. This phenomenon, called layover, occurs when SAR sensors are imaging a surface with a slope steeper than the incidence angle θ, such as the wall of a building. It is worth noting that

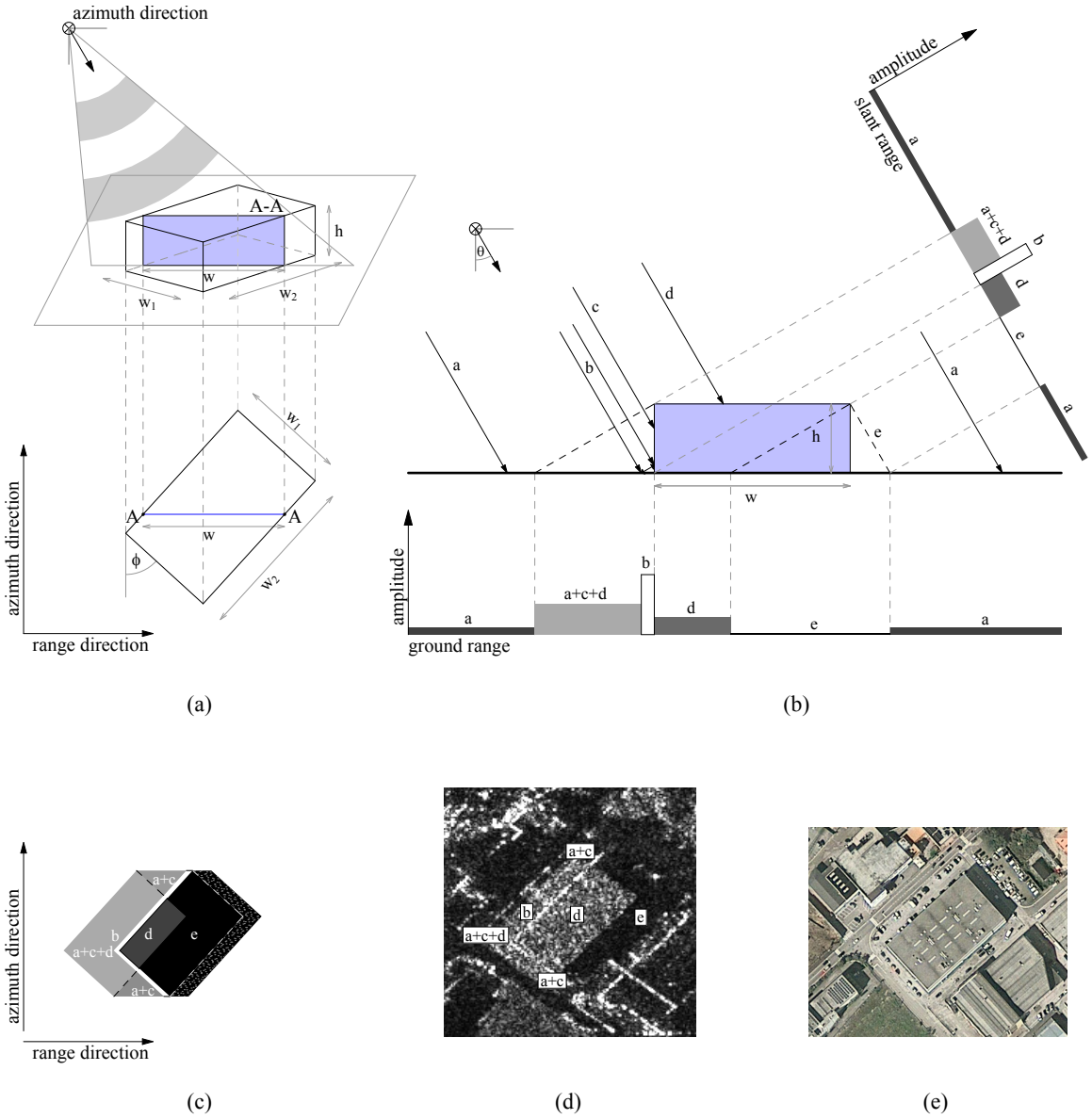

Fig. 1: Example of backscattering mechanism for a flat roof building. (a) Simplified model of a flat roof building oriented with a given aspect angle ϕ. The SAR sensor is moving on the left of the building. Theoretical scattering model for a given incidence angle θ in the case the sensor is illuminating: (b) only the section A-A of the building from a fixed position in the azimuth (the backscattering is reported in both slant and ground range); (c) the whole extension of the building (the backscattering is in slant range geometry). Different gray levels represent different amplitudes. Example of: (d) a real flat-roof building in Trento (Italy) acquired at 1 m resolution by TerraSAR-X in slant range (SAR illumination is from the left); (e) the same building in an optical image [36].

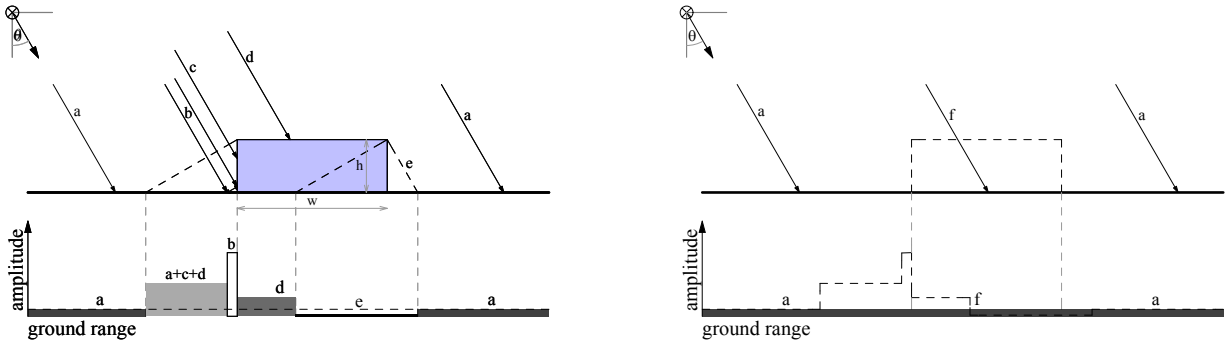

Fig. 2: Building scattering mechanisms for a fixed illumination source corresponding to: (a) a section of a building; (b) bare ground. The comparison of Figures (a) and (b) describes the multitemporal scattering mechanism in the case (a) a new building is built up (the envelope of backscattering of bare soil is reported for comparison in dotted line); and (b) a building is dismissed (the envelope of backscattering of the building in (a) is reported in dotted line).

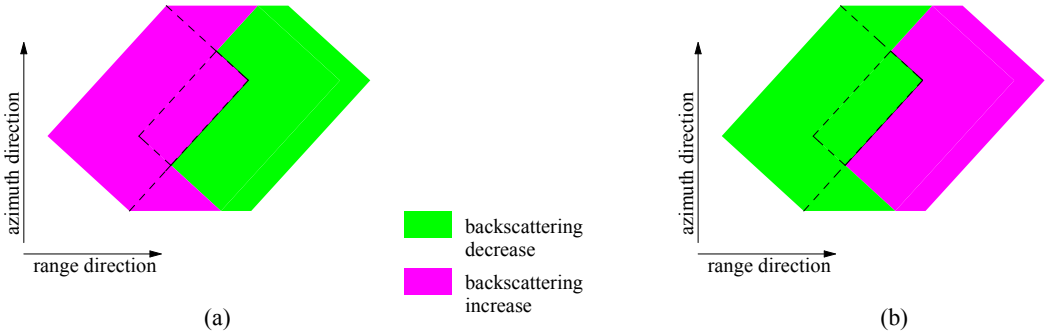

Fig. 3: Building scattering mechanisms in multitemporal VHR SAR images (illumination source on the left). Idealized map highlighting decrease and increase in the value of backscattering (unchanged pixels are in white) obtained in the case of (a) new and (b) fully demolished building.

the length of the layover, the roof contribution and the shadow depends on the width (w) and the height (h) of the section A-A, and the incidence angle θ.

In order to derive the appearance of the whole building in a VHR SAR image it is necessary to perform the aforementioned analysis for all the sections parallel to A-A that form the building. Nevertheless, as the width of each parallel section changes, the length of each mentioned contribution changes accordingly. Three cases can be observed on the basis of the relationship between the width w of the section A-A and the limit value w_b defined as [29], [38]:

$$w_b = \frac{h}{\tan\theta} \tag{1}$$

where h and θ are the height and the incidence angle of the building, respectively. Fig 1a shows the case in which

$w > w_b$. As the width of the section w decreases, the layover and shadow result larger whereas the backscattering from the roof will be absorbed in the layover. This behavior is valid up to the limit condition $w = w_b$ for which the whole roof contribution is sensed in the layover area before the double-bounce. In the case $w < w_b$ two contributions to layover areas can be distinguished: one due to the ground, the front wall and the roof ($a + c + d$), and one due to the backscattering from the ground and the front wall of the building ($a + c$). Fig. 1c shows the radar building footprint[1] generated from the building of Fig. 1a. It is a convex polygon made up of: i) a bright L-shaped region due to the layover; ii) a dark L-shaped region due to the shadow; iii) a bright L-shaped line due to the double bounce; iv) a rectangular region due to the direct return from the roof; and v) two bright triangular regions due to the layover of only ground and wall ($a+c$). It is worth noting that, since in the acquisition phase the radar is moving, the shadow casted by a ground object is moving as well resulting in a blurring of the border of the shadow [39], [40] (see the dotted area in Fig 1c). By comparing Fig. 1c and Fig. 1d it is possible to observe that the geometrical optics approximation can effectively describe the real behavior of scattering in VHR SAR images.

The same building may appear differently in SAR images according to the value of the aspect angle ϕ. When ϕ is approaching the limit values $\phi = 0°$ and $\phi = 90°$ the layover, the double bounce and the shadow change by approaching a rectangular shape. A special attention has to be given to the double bounce line with respect to the variation of ϕ [8], [9]. In [26] an empirical study on the relationship between the strength of the double bounce and the aspect angle highlighted that the double-bounce contribution drops off significantly if the aspect angle increases from $\phi = 0°$ up to $10°$, whereas it decays moderately for higher angles. θ also affects the appearance of a building in VHR SAR images. By reverting Eq. (1), it is possible to derive a limit value θ_b that is equivalent to w_b. Nonetheless, in urban areas the choice of θ can be critical for two reasons: i) the value of backscattering is related to θ i.e., small value of θ generates higher value of backscattering and vice-versa; and ii) a large value of θ generates long shadow areas and small layover areas, and vice-versa. Thus, the backscatter has a dependence on the incidence angle, and there is potential for choosing optimum configurations for different applications.

The same analysis described in this section for flat-roof building can be conducted for other building models e.g., gable-roof buildings [16]. The outcomes of such a study can be summarized as follows: the footprint of any type of isolated buildings with a rectangular base is given by a specific convex pattern made up of a bright area (due to layover and double bounce effects) followed by a dark area (due to the shadow effect). These features may have different thickness, shape and internal variability of backscattering on the basis of the considered building structure and material. Nevertheless they will systematically arise when SAR systems are sensing an isolated building with an adequate resolution.

B. Building Backscattering Mechanisms in Multitemporal VHR SAR Images

The aim of this section is to analyze the behavior of the radar backscattering in multitemporal images when a building changes by taking into account the single data analysis carried out in the previous section. This analysis

[1]Differently from [34] here with the term footprint we always refer to the radar footprint of a building.

introduces the basic concept on which the proposed approach is based. In order to properly illustrate the problem, let us focus on a building that fully disappears between two acquisitions. Let us assume to sample this situation acquiring one image when: i) the building is standing; and ii) the building is totally dismissed. Let us assume to use a VHR SAR system configured with the same geometrical parameters (i.e., same incidence angle θ and same azimuth path) for the two acquisitions. As in Section II-A, let us start the analysis by comparing the backscattering considering the illumination source fixed at a given point along the azimuth direction corresponding to section A-A (Fig. 1.a) in the case the building is present. The backscattering profile obtained for the standing building is reported in Fig. 2a. As one can notice, the backscattering behavior is the same as the one obtained in the previous section and reported in Fig. 1b. Whereas for the case of totally dismissed building, by assuming bare ground as depicted in Fig. 2b, the value of backscattering is approximately constant. By comparing Fig. 2a and Fig. 2b one can observe that the region with a high value of backscattering due to the layover $a + c + d$, the double bounce b, and the roof contribution d decreases its value when the building disappears, whereas the region hidden by the shadow e becomes visible to the line-of-sight of the radar and therefore increases its value (the dashed line in Fig. 2a represents the envelope of backscattering of bare ground). In other words, in the case of a new building we are likely to observe a structured pattern made up of two regions having increase and decrease of the backscattering oriented from near-to-the-far-range. Vice-versa if we consider the case in which a building disappears between two acquisitions, we expect that a structured pattern made up of two regions having decrease and increase in the backscattering values arises in near-to-the-far-range (the dashed line in Fig. 2b represents the envelope of the backscattering amplitude of a building).

This specific multitemporal behavior obtained when the illumination source is fixed at a given position in azimuth can be used to retrieve the appearance of new/demolished buildings in multitemporal VHR SAR images by repeating the same analysis for all the sections parallel to A-A that form the scene. The obtained new/destroyed radar building footprint is made up of a pattern included in a convex polygon. The pattern includes two regions that can be classified as: i) area of increase of the value of backscattering and, ii) area of decrease in the value of backscattering. The order of appearance of these two regions along the near-to-far-range direction defines if the pattern is due to new buildings (see Fig. 3a) i.e., the increase area (in this work depicted conventionally in magenta) is closer to the sensor than the area of decrease (in this work depicted conventionally in green), or demolished building (see Fig. 3b) i.e., the decrease area is closer to the sensor than the increase area.

By taking into account the analysis done in section II-A on the radar signature of a general isolated building it is possible to derive the appearance of the radar footprint of any type of newly built up or destroyed buildings in VHR SAR multitemporal images. In detail, the change radar building footprint can be identified checking: i) the presence of both the regions of increase and decrease in backscattering; ii) the proportion between the areas (in pixels) of the regions of increase and decrease in backscattering. The proportion depends on the incidence angle of the acquisition; iii) the equality between the lengths of the regions of increase and decrease in backscattering in the azimuth direction; iv) the alignment of the regions of increase and decrease in backscattering with respect to the range direction i.e., the barycenters of the two regions lay on the line with the range (As the regions in the

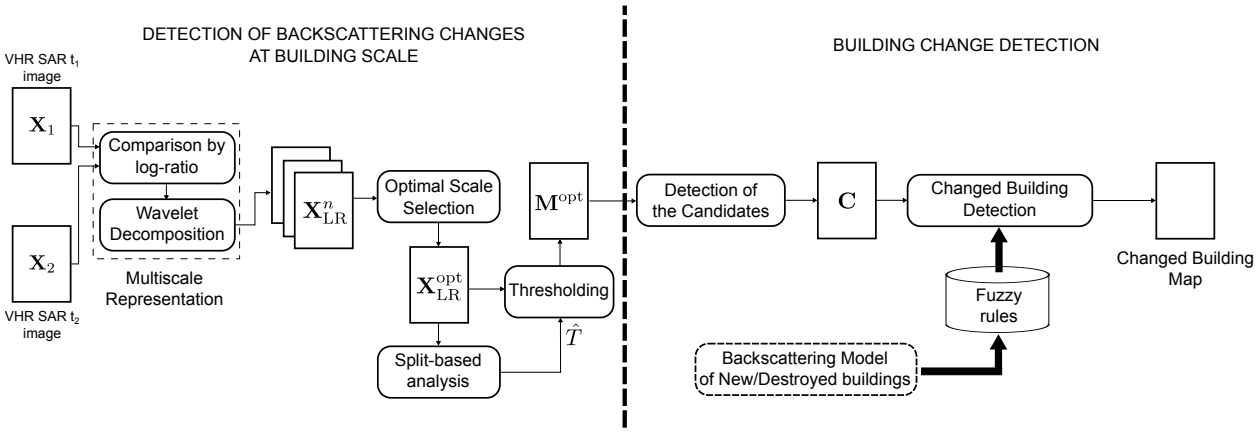

Fig. 4: Architecture of the proposed approach to building change detection.

model are not regularized the barycenters were calculated by means of the geometric decomposition method). The order of appearance of the two regions of increase and decrease in backscattering value determines if the changed radar building footprint is due to a new or a destroyed building.

It is worth noting that the regions of change may have different thickness, shape and variability of backscattering change on the basis of the considered building structure and acquisition geometry. Despite this variability, the pattern will systematically arise when SAR systems are sensing an isolated building with an adequate resolution [27]. Hence, a method for the detection of the changed building based on this concept results to be robust to both the noise and the uncertainty (i.e., the impossibly of modeling the reality precisely as described in Section III-D) of multitemporal VHR SAR data.

III. Proposed Building Change Detection Approach

Let us consider two amplitude VHR SAR images $\mathbf{X}_1$ and $\mathbf{X}_2$ of size $I \times J$ acquired with the same incidence angle on the same geographical area at different times τ_1 and τ_2, respectively. Let $\Omega = \{\omega_u, \Omega_c\}$ be the set of classes of changes to be identified: ω_u represents the class of pixels having unchanged backscattering value, whereas $\Omega_c = \{\omega_{c1}, \omega_{c2}, \ldots, \omega_{cK}\}$ is a meta-class that gathers all the K possible classes (kinds) of change that may arise on the ground. One of the most critical issues dealing with this kind of scenario is related to the presence of many kinds of changes on the ground. Nevertheless in this work we are interested to investigate an urban area with the goal to only detect changed buildings. In detail, we consider $K = 4$ classes of change: i) fully destroyed buildings (ω_{c1}); ii) new buildings (ω_{c2}); iii) changes that have a size comparable to a building but do not present the typical pattern of full new/demolished buildings (ω_{c3}); iv) all the other changes that do not show a size comparable to a building and are therefore not related to changed buildings (ω_{c4}). In order to achieve this classification we introduce an approach made up of two stages: i) identification of the areas affected by changes in the backscattering at the scale of buildings; and ii) exploitation of the backscattering models presented in Section II-B in order to detect the classes $\Omega_c = \{\omega_{c1}, \omega_{c2}, \ldots, \omega_{c4}\}$. Each stage of the proposed method is explained in detail in the next subsections.

Fig. 4 shows the block scheme of the proposed approach.

A. Detection of Backscattering Changes at Building Scale

As described in Section II-B, under the hypothesis of using a SAR sensor with a resolution comparable to the building size, the signature of isolated new/demolished buildings in multitemporal data is given by a pattern made up of increase and decrease of backscattering regions. The first stage of the proposed approach is thus devoted to extracting the areas that present whether a significant increase or decrease in the backscattering value. Nonetheless, at a resolution of a meter or less the small objects that form the buildings such as windowsills, or rain drains are visible. This results in an inhomogeneous signature of the building, which may affect also the appearance of new/destroyed buildings in multitemporal images rendering the regions of increase and decrease far from being homogeneous. Therefore, an optimum scale level for representing buildings, and not sub-parts of them, has to be derived from the VHR images and used to identify the regions of increase and decrease of backscattering. Working at the scale level of buildings has the additional advantages of: i) reducing the impact on the detection of small changes and thus reducing the false alarm rate; ii) making it possible a mitigation of the speckle effect on the detection.

In order to work at the scale of a building we propose to build a multiscale representation of the multitemporal information made up of N scale level. The $(N-1)^{\text{th}}$ resolution level, which represents the optimum scale level, is select according to the minimum size of the building in the investigated scene. The multiscale representation can be obtained by applying several methods e.g., Laplacian/Gaussian pyramid decomposition [41], or Wavelet transform [42]. Here the two-dimensional discrete stationary wavelet transform (2D-SWT) is exploited, which has the advantage of avoiding the down-sampling after each convolution step [43]. In detail, we used the Wavelet-based decomposition and reconstruction of the log-ratio image approach presented in [44] for change detection in medium resolution SAR images. The log-ratio image $\mathbf{X}_{\text{LR}}$, which is derived as $\mathbf{X}_{\text{LR}} = \log \mathbf{X}_2/\mathbf{X}_1$, efficiently points out the differences in backscattering values. In $\mathbf{X}_{\text{LR}}$ unchanged pixels assume values close to zero, whereas increase and decrease of backscattering assume positive and negative values far from zero, respectively. This is the most common way for highlighting changes in multitemporal SAR data [45], [46]. From $\mathbf{X}_{\text{LR}}$ a set of multilevel images $\mathcal{X}_{\text{MS}} = \left\{\mathbf{X}_{\text{LR}}^0, \ldots, \mathbf{X}_{\text{LR}}^n, \ldots, \mathbf{X}_{\text{LR}}^{N-1}\right\}$ is computed, where the superscript n, $n = 0, \ldots, N-1$, indicates the resolution level. This is done in two steps: a decomposition phase in which $\mathbf{X}_{\text{LR}}$ is filtered through a cascade of n filters, and a reconstruction phase in which only the information of interest is used to reconstruct the original image at the n^{th} resolution level. According to [44], the decomposition is based on 2D-SWT, which applies to the considered image appropriate level-dependent high- and low-pass filters at each resolution level n. Filter impulse response depends on the selected Wavelet family. For each approximation sub-band $\mathbf{X}_{\text{LR}}^{\text{LL}_{n+1}}$ the inverse stationary wavelet transform (2D-ISWT) is applied $n+1$ times in order to reconstruct in the image space the set $\mathcal{X}_{\text{MS}} = \left\{\mathbf{X}_{\text{LR}}^0, \ldots, \mathbf{X}_{\text{LR}}^n, \ldots, \mathbf{X}_{\text{LR}}^{N-1}\right\}$. For n ranging from 0 to $N-1$, the images are characterized by resolution that is degraded approximately by a factor of 2^n. Therefore, as expected by decreasing the resolution, small changes tend to disappear and only changes of a given size are fully preserved. More details on this strategy are given in [44].

Once the optimum scale level (opt) has been selected, a change detection (CD) map $\mathbf{M}^{\mathrm{opt}}$ is derived from $\mathbf{X}_{\mathrm{LR}}^{\mathrm{opt}}$ according to an unsupervised thresholding procedure. $\mathbf{M}^{\mathrm{opt}}$ presents three classes: i) no-change (ξ_u); ii) increase (ξ^+); and iii) decrease (ξ^-) of backscattering. As the analysis of large urban areas with VHR SAR sensors leads to the generation of large multitemporal images it is possible that the population of changed pixels is in sharp minority in the full $\mathbf{M}^{\mathrm{opt}}$. This may affect the accuracy of the threshold selection technique. In order to address this issues we adopt the thresholding method presented in [47]. This method divides the considered image into sub-images of a given size (splits) and performs the threshold selection considering only the splits that present the highest probabilities to contain changed pixels. This selection allows the definition of a subset of pixels in which the class of change shows a higher prior probability than in the whole image. For our purpose, $\mathbf{X}_{\mathrm{LR}}^{\mathrm{opt}}$ is split into a set of S sub-images of a user-defined size. The choice of the split size $S_R \times S_A$ is driven by the average extension of the expected changes. Since we are considering changes related to buildings, we can determine S_R and S_A taking into account the average size of the radar footprint of the changed buildings in the considered radar image. This information can be inferred by considering the actual average size of the buildings i.e., w_1, w_2 and h (see Fig. 1a) in the considered area and converting it into SAR geometry by applying the following equations[2] [38]:

$$S_R = X + Y = \begin{cases} w_1 \sin\theta + \frac{h}{\cos\theta}, & \text{if } \theta \geq \tan^{-1}(\frac{h}{w_1}) \\ h\cos\theta + (w_1 + \frac{h}{\tan^{-1}\theta})\sin\theta & \text{Otherwise.} \end{cases} \tag{2}$$

$$S_A = w_2 \tag{3}$$

Where X is the length of the return from the building (i.e., the sum of the lengths of contributions ($a+c+d$), b and d of Fig. 2.a) and Y the length of the shadow (i.e., the length of contribution e in Fig. 2a). Once the sizes S_R and S_A are defined, the splits are identified and selected according to their probability to contain a significant amount of changed pixels. The selection is done according to the value of the variance σ_s^2, $s = 1, \ldots, S$, computed on the pixels of each split. This is a reasonable index for predicting the presence of changes in the log-ratio image since the residual multiplicative noise of the ratio image becomes additive due to the log operator. The desired set $\mathcal{P}_S$ of splits with the highest probabilities to contain changes is defined by selecting the splits that satisfy the following inequality:

$$\sigma_s^2 \geq \bar{\sigma}^2 + B\sigma_{\sigma^2}, \quad s = 1, \ldots, S \tag{4}$$

where $\bar{\sigma}^2$ denotes the average variance of splits, σ_{σ^2} is the standard deviation of the variance of splits, and $B > 0$ is a constant. High values of B results in the selection of only those splits with high variance (i.e., the ones with the highest probability to contain changes); vice-versa, low values of B results in the selection of more splits. The split-based selection allows defining a subset of pixels $\mathbf{X}_{\mathrm{s}} = \{\mathbf{X}_{\mathrm{LR}} | \mathbf{X}_{\mathrm{LR}} \in \mathcal{P}_S\}$ in which the classes of change show a higher prior probability than in the whole image. Consequently, the statistical estimation of the parameters related to

[2]Eq. (2) and Eq. (3) hold assuming flat-roof buildings with rectangular layout and SAR images in slant range geometry.

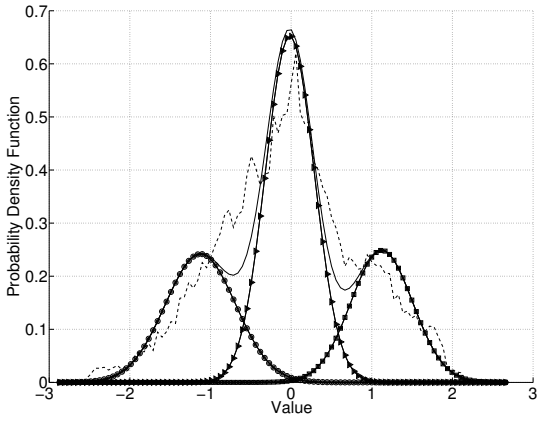

Fig. 5: Probability density function estimated from the pixels of the selected splits $\mathbf{X}_{\mathrm{s}}$ using a mixture of three Gaussians (solid line) compared with rescaled histogram of the pixels of the selected splits $\mathbf{X}_{\mathrm{s}}$ (dashed line). Estimated distributions of the classes of no-change, decrease in backscattering and increase in backscattering are reported with line marked with triangles, circles and squares, respectively.

the three probability density functions associated with no-change, increase, and decrease of backscattering between the two dates (i.e., ξ_u, ξ^+, ξ^-), can be correctly derived and used to separate the three classes. Fig. 5 depicts an example of the gaussian mixture probability density function (pdf) estimated from $\mathbf{X}_{\mathrm{s}}$, which are extracted from real VHR SAR data. As one can notice the three modes associated to three classes ξ_u, ξ^+, ξ^- are discernible by means of two thresholds $\hat{t}^+$ and $\hat{t}^-$. Here the thresholding method described in [48] is adopted and the Bayes decision rule for minimum error is applied to separate the 3 classes. To this end a statistical model for class distributions is required together with an approach for class statistical parameters estimation. The Gaussian model and the well known Expectation-Maximization (EM) algorithm [49] are employed to derive $\mathbf{M}^{\mathrm{opt}}$.

In Fig. 6 an illustrative example that depicts the detection process of the proposed approach is reported for the case of a demolished building. This example will be used in the paper to better illustrate the proposed approach. As one can notice, in this example the CD map $\mathbf{M}^{\mathrm{opt}}$ reported in Fig. 6a verifies the assumptions defined for the model presented in Section II-A: i) the detected regions of increase or decrease in backscattering at the building scale are homogeneous; and ii) the change detection map presents a reduced number of changes smaller than the size of buildings i.e., changes that are not related to changed buildings (ω_{c4}) are filtered out. From $\mathbf{M}^{\mathrm{opt}}$ it is possible to identify the building radar footprints by locating the pattern of increase and decrease of backscattering (building candidates) and by evaluating the matching between the properties of the building candidates with respect to the properties of new and destroyed building models described in Section II-B. This task is preformed by the building detection stage of the proposed approach and it will be described in detail in the following section.

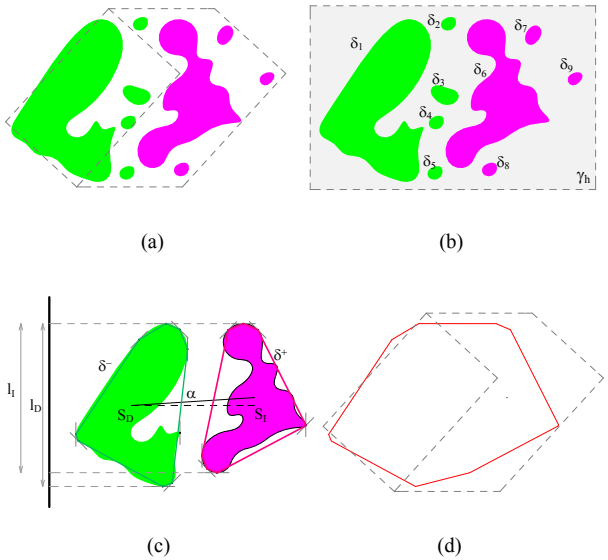

Fig. 6: Conceptual example of detection of a destroyed building (illumination source on the left). (a) $\mathbf{M}^{\mathrm{opt}}$. The pixels associated to the classes of backscattering decrease (ξ^{-}) and increase (ξ^{+}) are reported in green and magenta, respectively. The idealized dismissed radar building footprint is drawn in dashed line; (b) in gray the bounding box of changed building candidate γ_h containing the regions of change $\delta_1, \delta_2, \ldots, \delta_8$ that form the candidate; (c) illustration of the parameters S_I, S_D, l_I, l_D and α, which are evaluated by the fuzzy rules described in Table I in order to check the matching between the candidate and the expected pattern; (d) identified demolished radar building footprint (red continuous-line) compared with the actual radar footprint (gray dashed-line).

B. Building Change Detection

This stage of the proposed approach represents the most novel contribution of this work and it is devoted to the detection of demolished building (ω_{c1}), new buildings (ω_{c2}), changes that have a size comparable to a building but do not present the typical pattern of full new/demolished buildings (ω_{c3}) and all the other changes that do not show a size comparable to a building and are therefore not related to changed buildings (ω_{c4}). To this end a procedure based on two steps is developed. First the areas of change candidate to be associate to one of the classes ω_{c1}, ω_{c3} or ω_{c3} (changed building candidate) are detected among all the backscattering changes highlighted in $\mathbf{M}^{\mathrm{opt}}$. The set of changed building candidates is denoted by $\Gamma = \{\gamma_1, \gamma_2, \ldots, \gamma_H\}$. Then the matching between the expected backscattering behavior of changed buildings (presented in Section II-B) and the characteristics of the changed building candidates is evaluated. This is done by considering the physical properties and the relation of the regions of change inside each candidate i.e., $\Delta = \{\delta_1, \delta_2, \ldots, \delta_K\}$. In order to properly model the uncertainty inherent in the process (that can be due for example to cluttered objects placed in front of buildings) fuzzy theory is used [50]. Fig. 6b-d illustrates the process of the proposed building change detection stage for the case of a demolished building. In the following each step is described in detail.

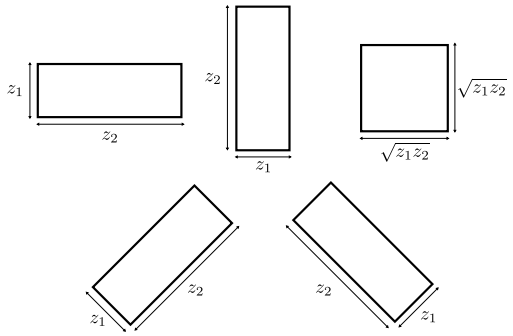

Fig. 7: Windows used to derive the changed building candidates.

The first step of the change detection phase aims at detecting the set of changed building candidates $\Gamma = \{\gamma_1, \gamma_2, \ldots, \gamma_H\}$. Ideally each changed building in $\mathbf{M}^{\text{opt}}$ is made up of regions of both increase and decrease in backscattering, whose total extension is comparable with the expected size of buildings. One simple and effective approach to identify the changed building candidates $\gamma_1, \ldots, \gamma_H$ is to use a sliding window algorithm for each pixel in the image. Pixels within a window around it are taken and used to compute the detector output. In this work, the window is moved in $\mathbf{M}^{\text{opt}}$ from left to the right by one pixel and the number of changed pixels (labeled both as increase ξ^+ or decrease ξ^-) is counted. The process is repeated over 5 moving windows: four rectangular moving window showing different directions and a square window having the same area of the rectangular ones. This choice allows us to properly capture the most of the building orientations. The detector output is given by the window that results in the maximum value. The 5 windows are depicted in Fig. 7. The size of the windows $z_1 \times z_2$ is chosen according to the minimum size of the buildings in the considered scene in order to minimize missed alarms. Hence, let $\mathbf{M}^{\text{opt}}_{W^{\beta}_{i,j}} = \{\mathbf{M}^{\text{opt}} | \mathbf{M}^{\text{opt}} \subset \mathbf{W}^{\beta}_{i,j}\}$ be the set of pixels of $\mathbf{M}^{\text{opt}}$ included in the windows $\mathbf{W}^{\beta}_{i,j}$ centered at the pixel (i,j), with $\beta = 1, \ldots, 5$ indicating the different windows. Let $\mathbf{C}$ be the image with size $I \times J$ that reports for each pixel $C_{i,j}$ an index of the size of the changes. $C_{i,j}$ is computed as the maximum on the five windows as follows:

$$C_{i,j} = \underset{\beta \in 1,2,\ldots,5}{\arg\max} \left\{ \left| \mathbf{M}^{\text{opt}}_{\mathbf{W}^{\beta}_{i,j}} \in \xi^+ \vee \mathbf{M}^{\text{opt}}_{\mathbf{W}^{\beta}_{i,j}} \in \xi^- \right| \right\} \quad \forall \quad i = 1, \ldots, I; \quad j = 1, \ldots, J. \tag{5}$$

where $|\cdot|$ indicates the cardinality of a set. The obtained index image $\mathbf{C}$ exhibits relatively high values when the sliding window contains a large amount of changes oriented in the same direction of the moving window. $\mathbf{C}$ exhibits relatively low values when the sliding window contains small changes and when the windows does not match the orientation of the change. Therefore, it is possible to detect the changed areas that can be associated in terms of size to the expected radar footprint of changed buildings by selecting the areas of $\mathbf{C}$ exceeding a certain threshold

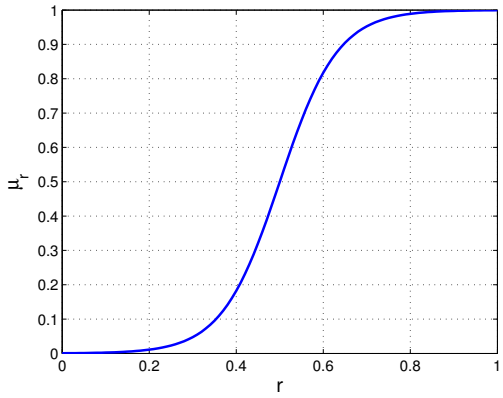

Fig. 8: Example of sigmoid function $\mu_r(r)$ defined according to (7). The slope of the sigmoid is tuned by the parameter a_i. b_i defines instead the center of the sigmoid i.e., $\mu_r(b_i) = 0.5$. In the represented case $a_i = 15$ and $b_i = 0.5$.

T_C, thus obtaining the image $\bar{\mathbf{C}}$ as follows:

$$\bar{\mathbf{C}} \in \begin{cases} 1, & \text{if} \quad \mathbf{C} \geq T_C \\ 0, & \text{otherwise.} \end{cases} \tag{6}$$

T_C is selected according to the expected minimum size of buildings $z_1 \times z_2$ in the investigated scene. The map $\bar{\mathbf{C}}$ represents the areas containing changes with size comparable or bigger than the minimum building size and therefore they belong to one of the classes $\omega_{c1}, \omega_{c2}, \omega_{c3}$. As one can notice, the pixels belonging to ω_{c4} are implicitly identified in this operation. From the map $\bar{\mathbf{C}}$ the set of changed building candidates $\Gamma = \{\gamma_1, \gamma_2, \ldots, \gamma_H\}$ is extracted by calculating the connected components considering a 8-connected neighborhood. This is done by means of a flood-fill algorithm [51]. Each candidate γ_h $(h = 1, \ldots, H)$ contains a subset of regions $\Delta = \{\delta_1, \delta_2, \ldots, \delta_K\}$ labeled as ξ_u, ξ^+ or ξ^-. The information associated to the kind of change is derived considering $\mathbf{M}^{\text{opt}}$ in the areas delimited by the region γ_h. Fig. 6b shows an example of candidate γ_h that contains δ_k $(k = 1, \ldots, 8)$ regions for the case of a demolished building. In general the number of regions, k may vary from 1 to K depending on the size and proximity of the changes. For the sake of clarity, in the next step of the building change detection procedure we assume that only two regions belonging to increase (i.e., $\delta^+ = \delta_k \in \xi^+$) or decrease i.e., ($\delta^- = \delta_k \in \xi^-$) occur inside a candidate. If more than 2 regions are present, all the combinations among the regions of increase and decrease are automatically analyzed by the proposed approach and the most reliable(s) selected.

In order to properly classify each changed building candidate according to the classes ω_{c1}, ω_{c2}, and ω_{c3}, the physical characteristics and the spatial arrangement of the pattern formed by the regions δ_k $(h = 1, \ldots, K)$ have to match with the four characteristics of the models of new or dismissed building discussed in Section II-B. The matching is tested exploiting four fuzzy rules called here: completeness, proportionality of areas, equivalence of lengths and alignment. These rules aim at associating a grade of membership to the changed building candidate for

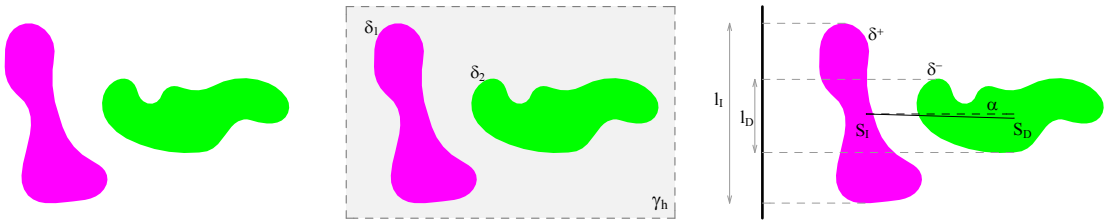

(a) (b) (c)

Fig. 9: Example of a candidate γ_h that does not respect the equivalence of lengths. (a) $\mathbf{M}^{\text{opt}}$. The pixels associated to backscattering decrease (ξ^-) and increase (ξ^+) classes are reported in green and magenta, respectively. (b) In gray the changed building candidate γ_h containing the regions δ_1 and δ_2, which form the candidate; (c) Analysis of psychical properties and relations of the regions δ^+ and δ^-.

each of specific performed test. On the basis of the aggregate membership the final classification decision is taken. In the following each rule is presented in detail.

1) Completeness: A pair of regions of increase and decrease is strictly needed to identify a new (ω_{c2}) or destroyed building (ω_{c1}). The first rule evaluates the simultaneous presence of δ^+ and δ^- inside the candidate γ_h. This is done by means of a crisp membership function μ_p that takes value 0 or 1 ($\mu_p(p) = \{0, 1\}$) depending on whether regions of increase and decrease are simultaneously present $\mu_p(p) = 1$ or not $\mu_p(p) = 0$.

2) Proportionality of Areas: This rule aims at verifying that the area δ^+ is not prevailing with respect to the area of δ^-, and vice-versa. The mathematical modeling of this rule depends on the parameters of acquisition and the size of the building as discussed in Section II-A. It can be effectively represented by a sigmoid membership function that evaluates the attribute $r_s = \min\{s_I/s_D, s_D/s_I\}$, where s_I and s_D indicate the areas of δ^+ i.e. $S_I = |\delta^+|$ and δ^- i.e., $S_D = |\delta^-|$, respectively. In general, a sigmoid function is defined as follows:

$$\mu_r(r) = \frac{1}{1 + e^{-a_i(r-b_i)}} \tag{7}$$

The constant a_i tunes the slope of function and the constant b_i locates the center of the function. Eq. 7 returns values in [0,1]. Fig. 8 shows an example of sigmoid function. In accordance with the model it is expected that the smaller is r_s the smaller is the membership grade of the candidate hence for this rule $a_i = a_1 > 0$ and $b_i = b_1 > 0$.

3) Equivalence of Lengths: This rule aims at checking that the lengths of the regions δ^+ and δ^- in the azimuth direction are equivalent. This is done by identifying the extrema of the regions δ^+ and δ^-. To test the reliability of a candidate with respect to this criterion, the attribute $r_l = \min\{l_I/l_D, l_D/l_I\}$ (where l_I and l_D are the lengths in azimuth direction of δ^+ and δ^-, respectively) is used in the sigmoid membership function defined in eq. (7) with parameters $a_i = a_2 > 0$ and $a_i = b_2 > 0$. Since the farther is r_l from 1 the smaller is the membership grade of the candidate to be associated to a new/destroyed building, the slope of the sigmoid is steep and the center moved toward 1. Fig. 6.c illustrates an example of correct alignment between δ^+ and δ^-, whereas Fig. 9c depicts a case in which this rule is not satisfied.

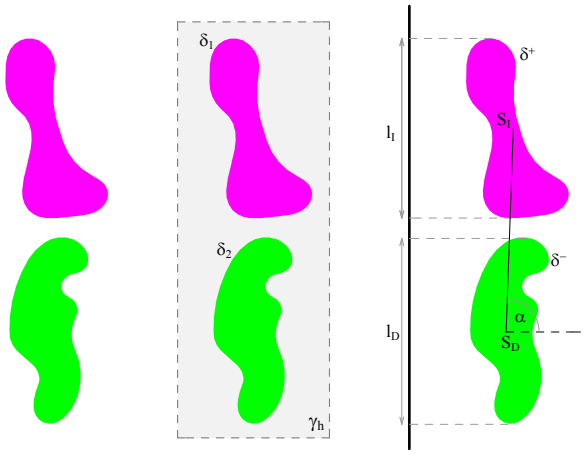

(a) (b) (c)

Fig. 10: Example of a candidate γ_h that does not respect the fourth rule. (a) $\mathbf{M}^{\mathrm{opt}}$. The pixels associated to backscattering decrease (ξ^-) and increase (ξ^+) classes are reported in green and magenta, respectively. (b) In gray the changed building candidate γ_h containing the regions δ_1 and δ_2, which form the candidate; (c) Analysis of psychical properties and relations of the regions δ^+ and δ^-.

4) Alignment: This rule is devoted to test the alignment of the entire pattern increase/decrease (which is made up of regions δ^+ and δ^-) with respect to the range direction. The alignment of the centroids of the regions of increase and decrease are considered, which are expected to lay on the same line. In detail, the absolute value of the angle α defined as the angle included by the line that connects the centroids of the regions δ^+ and δ^- and the SAR range direction is used in the equation of the sigmoid eq. (7). α ranges from $[-\pi/2, \pi/2)$. As expected, by imposing $a_i = a_3 < 0$ the larger is $|\alpha|$ the smaller is the membership grade of the candidate to be associated to a new/destroyed building. Fig. 6c illustrates an example of correct orientation of the pattern increase/decrease, whereas Fig. 9c depicts a case in which this rule is not satisfied.

A summary reporting the description of each rule, the parameters and membership functions used to represent the rules is reported in Table I.

The final decision on the label of the candidate is done according to the aggregated membership grade M, which is calculated by combining the 4 membership functions. Among the fuzzy aggregation methods presented in the literature in this work the Larsen product implication [52] is used i.e.,

$$\mathrm{M} = \mu_p \mu_{rs} \mu_{rl} \mu_\alpha \tag{8}$$

In this way we apply a conservative rule for which one small value among the individual membership grades yields the final result to be small regardless of the other values (other rules can be selected [50]). The candidates that present a value of M greater than a user-defined threshold T_{M} are selected as fully demolished (ω_{c1}) or new buildings (ω_{c2}) considering the order of appearance of the pair increased/decreased with respect to the range

TABLE I: Fuzzy rules used to classify γ_h as new building (ω_{c1}), demolished buildings (ω_{c2}) or change comparable to the size of a building but not related to fully new/demolished buildings (ω_{c3}).

Rule	Parameter	Membership Function
1. Presence of both regions δ^+ and δ^- (completeness)	p	$\mu_p(p) = \{0, 1\}$
2. Proportionality of areas of δ^+ and δ^- (proportionality of the areas)	$r_s = \min\left(\frac{s_I}{s_D}, \frac{s_D}{s_I}\right)$	$\mu_{r_s}(r_s) = \frac{1}{1+e^{-a_1(r_s-b_1)}}$
3. Equivalence of the lengths of δ^+ and δ^- along the azimuth direction (equivalence of the lengths)	$r_l = \min\left(\frac{l_I}{l_D}, \frac{l_D}{l_I}\right)$	$\mu_{r_l}(r_l) = \frac{1}{1+e^{-a_2(r_l-b_2)}}$
4. Alignment of the barycenters of the regions δ^+ and δ^- (alignment)	$\lvert\alpha\rvert$	$\mu_{\lvert\alpha\rvert}(\lvert\alpha\rvert) = \frac{1}{1+e^{-a_3(\lvert\alpha\rvert-b_3)}}$

direction as described in Sec. II-B. The others are classified as ω_{c3} (i.e., they are not fully demolished or new buildings). It is worth noting that T_{M} will be a small value since the algebraic product of value smaller than 0 result in value smaller than the factors in (8). Nonetheless, the value of M obtained for each of these classes is representing a grade of reliability of the detection that can be used by the final users.

For each changed building candidate recognized as new or demolished building the 8-extrema points (i.e., from top-left to bottom-right) of both the regions δ^+ and δ^- are calculated and used to find the smallest convex polygon that contains the two regions i.e., the convex hull (see Fig. 6d). The computation of the convex hull is done using the Quickhull algorithm [53]. This allows the generation of an envelope of a new or dismissed building footprint as much as similar to the ideal expected one. Once the building footprint candidate is classified as new or demolished building, reverting the equations (2) and (3) it is possible to estimate the actual size of the building affected by the change, which is expressed in terms of $w_1[m] \times w_2[m] \times h[m]$ (see Fig. 1a).

C. Selection of the Parameters

In this section the role of the parameters used in the proposed approach is discussed in detail. The parameters can be divided into 3 groups: the first two groups are related to the building size and the third to the fuzzy rules. The first group includes S_R and S_A, which represent the size of the split used for the automatic thresholding procedure of the log-ratio image at the optimal building scale. As discussed in the paper, the split size is selected according to the average size of building in the considered area. It is worth noting that the split-based thresholding approach has demonstrated to be tolerant to relative large variations of the selected split size with respect to the expect average size of buildings (see Sec. IV). The second group of parameters includes $N-1, z_1$, z_2 and T_C are related to the minimum size of the buildings in the investigated site. In general, the minimum size of buildings is driven by the typology of urban area (industrial or residential) and the zone of the world under analysis (e.g., typically buildings in US metropolis are larger than buildings in European towns). Nonetheless, by selecting large values of $N-1, z_1$, z_2 and T_C building candidates with size smaller than the chosen values can be excluded from the analysis. The third group of parameters is associated to the membership functions of the fuzzy rules. In detail the center of the sigmoids (regulated by b_1, b_2, b_3) represents the boundary situation that has half membership with respect to the

theoretical model described in Section II-B, while the slope (regulated by a_1, a_2, a_3) represents the flexibility of the rule to cope with clutter and noise. In the considered case the centers are fixed from the model, whereas the slope can be chosen considering real situations e.g., urban density.

On the basis of this analysis and of our experimental results we can conclude that the tuning of the parameters to give as input to the proposed approach requires very basic prior information and is not critical.

D. Critical Analysis

It is worth noting that, as discussed in Section II the appearance of a building in VHR SAR imagery can vary with respect to the model of the building. For instance, in the case discussed in Section II-A the area of the regions of increase and decrease of backscattering are similar to each other. This is not always the case as it depends on both the size of the building and the incidence angle θ used for the acquisition. Moreover, objects placed in front of the building, such as trees or other buildings, or the high urban building density results in the occlusion of neighboring of the building facade and the corner reflector so that the double bounce and the layover might not be visible for the full extent of the building front wall. As a consequence, important primitives that identify a building may be partially not visible reducing the validity of the aforementioned conditions. This challenging situation is taken into account in the proposed method by using the fuzzy theory. Moreover, note that the comparison of multitemporal images according to the log-ratio operator also mitigates the negative effects of possible occlusions common to both images. Accordingly, the proposed approach is expected to be more robust to non ideal conditions than methods based on the separate detection of buildings in single data images. Thus the proposed approach is robust against false and missed alarms as it will be discussed in the experimental results section.

As a matter of fact, the multitemporal analysis becomes complex if we consider the case of building partially damaged or under construction. In these cases the backscattering characteristics are dependent on the specific kind and the extension of the change. In [16], [54], [55] it was proven that not all kinds of building damages are discernible in meter resolution SAR imagery. This is valid also in the case of partially built buildings. At present this is still an open topic that will be further investigated as future development of this work.

IV. Data Sets Description and Experimental Results

In order to assess the effectiveness of the proposed approach, different experiments were carried out on two data sets. The first one is related to the 2009 L'Aquila earthquake occurred in the region of Abruzzo, in central Italy. The second one documents the urban evolution of the city of Trento, in north Italy, between 2011 and 2013.

A. 2009 L'Aquila Earthquake: Detection of Destroyed Buildings

The first data set is made up of two spotlight mode X-band CSK 1-look amplitude images processed according to the standard processing level 1C (Geo-coded ellipsoid corrected, 1m resolution, 0.5m$\times$0.5m pixel spacing). They were acquired in HH-polarization on April 5, 2009 and on September 12, 2009, over the city of L'Aquila ($42^\circ 21'$N


N

(a)

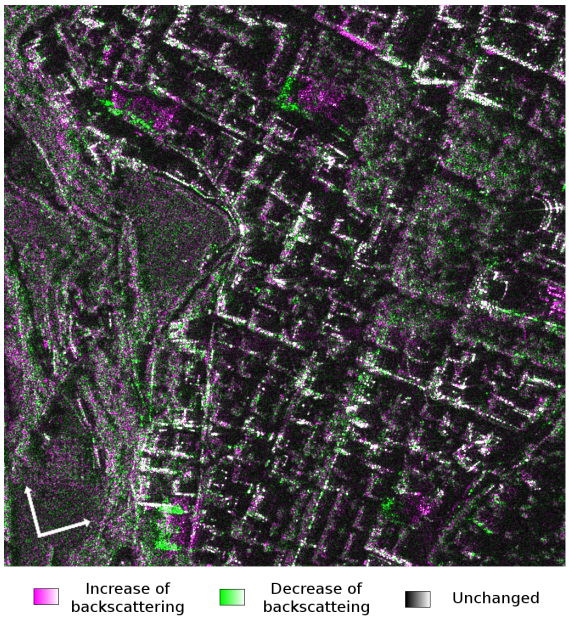
Increase of backscattering
Decrease of backscatteing
Unchanged

(b)

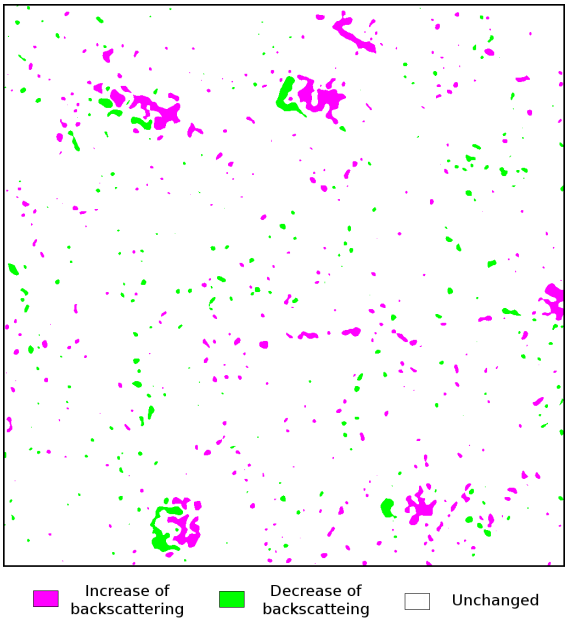
Increase of backscattering
Decrease of backscatteing
Unchanged

(c)

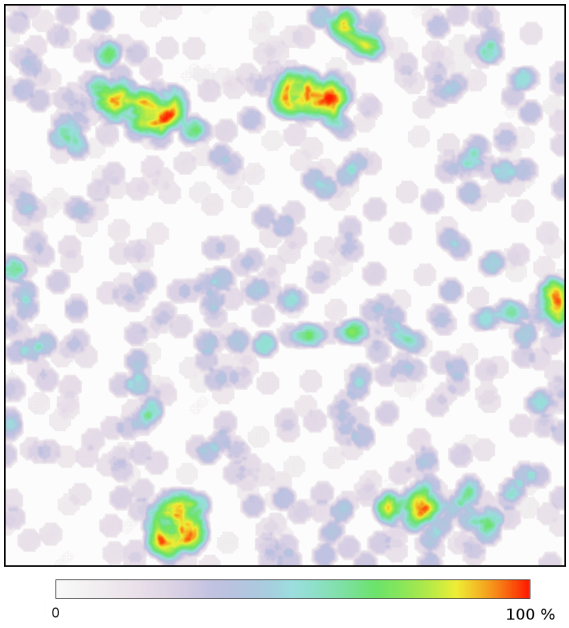
0
100 %

(d)

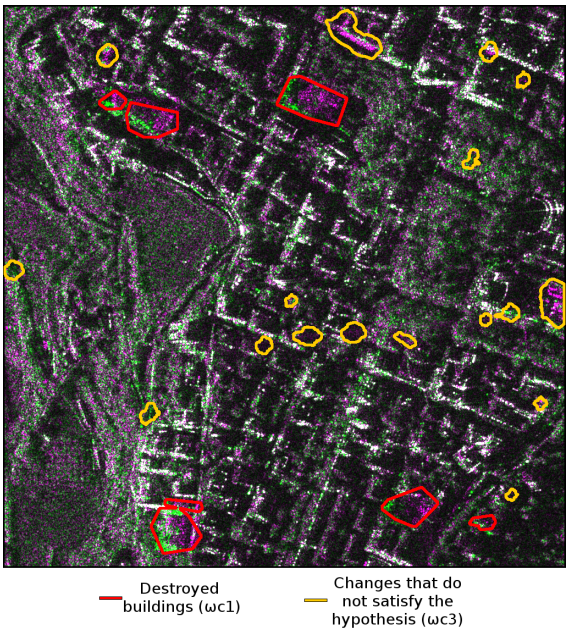

(e)

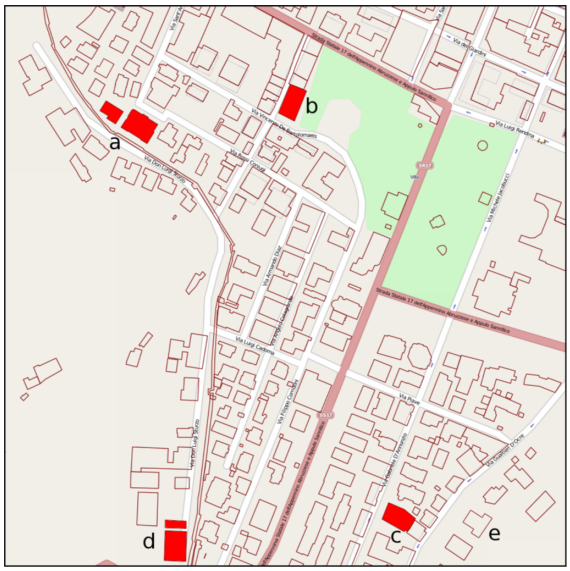

(f)

Fig. 11: L'Aquila (Italy) data set: (a) optical image. (September 4, 2006 [36]); and (b) RGB multitemporal composition of spotlight COSMOSky-Med images (R:09/12/2009, G:04/05/2009, B:09/12/2009). The images are geo-projected according to the reference ellipsoid. Actual range and the azimuth directions are reported in white arrows. (c) Change detection map $\mathbf{M}^{\text{opt}}$ obtained at the level $N-1=3$. (d) Map showing the index of the size of changes $\mathbf{C}$. (e) Changed building map overlapped to the RGB multitemporal composition of CSK data. (f) Cadastral map of the area (destroyed buildings are reported in red).

$13°24'$E) in ascending orbit with 57-58 degree incidence angle. On April 6, 2009, an earthquake of 6.3 Moment Magnitude Scale (MMS) struck central Italy with its epicentre near L'Aquila.

A test site of 1024×1024 pixels of the full spotlight scene was selected in the city of L'Aquila in order to test quantitatively the proposed method. Fig. 11a shows the optical image corresponding to the area of interest. Fig. 11b shows a false color composition of the two CSK images (red channel:09/12/2009, green channel:04/05/2009, blue:09/12/2009) in which pixels with an increase in the value of backscattering appears in magenta tone, pixels with a decrease in the value of backscattering appear in green tone and unchanged pixel in gray-scale. From the cadestrial map of the considered site 200 buildings were counted and 6 of them were identified as totally collapsed because of the earthquake. This information was derived by analyzing a couple of orthophotos with a resolution of about 20 cm acquired April 8, 2009 and October, 2009 [56]. It is worth noting that a relevant number of changes are present between the two acquisitions. Some of those are not relevant from the application viewpoint because they are due to the activities occurred after the earthquake (e.g., shoring up of damaged structures or deployment of emergency services). This increases the complexity of the problem of building change detection.

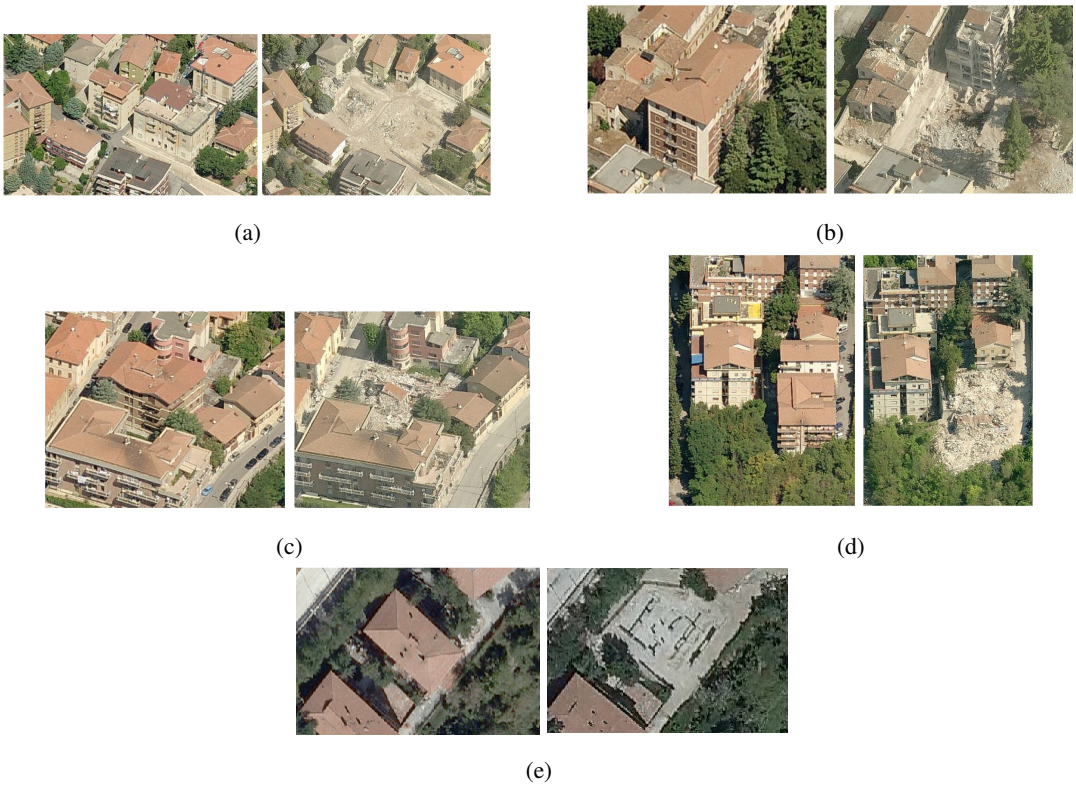

Fig. 12: (a)-(d) Zoom of the 6 buildings destroyed and correctly detected by the proposed method [57]. See Fig. 11f for the correspondence of the buildings on the map. (e) Zoom of the orthophotos on the building wrongly detected as destroyed. As one can notice building was totally demolished after the earthquake.

TABLE II: Performance of the proposed approach for L'Aquila Dataset in terms of number of detected destroyed buildings and missed destroyed buildings. The total number of buildings present in the site is also reported in the table.

Total Number of Buildings	Number of Destroyed Buildings (reference)	Detected Destroyed Buildings (ω_{c1})	Missed Destroyed
200	6	7	0

As described in the methodological part, the first step of the proposed approach is the calculation of the log-ratio image $\mathbf{X}_{\mathrm{LR}}$. It was computed from the two calibrated and co-registered CSK images. In detail, the co-registration was performed with sub-pixel accuracy and the radar brightness calibration was applied in order to render the two images comparable. From $\mathbf{X}_{\mathrm{LR}}$ the set $\mathcal{X}_{\mathrm{MS}} = \left\{\mathbf{X}_{\mathrm{LR}}^{0}, \ldots, \mathbf{X}_{\mathrm{LR}}^{n}, \ldots, \mathbf{X}_{\mathrm{LR}}^{N-1}\right\}$ was computed by applying sequentially the 2D-SWT and the 2D-ISWT with an 8-length *Daubechies* filter. The impulse response of low-pass decomposition *Daubechies* filter of order 4 is given by the following coefficient set:

$$\{-0.0105974, 0.0328830, 0.0308414, -0.187035,$$

$$-0.0279838, 0.630881, 0.714847, 0.230378.\} \tag{9}$$

The finite impulse response of the high-pass filter for the decomposition step can be computed by satisfying the properties of the quadrature mirror filters. The level $(N-1)^{\text{th}} = 3^{\text{rd}}$, which gives a resolution of approximately 8 meters, was selected as the optimum one. This allows to observe radar footprints of buildings as small as 8 by 8 meters, which is compatible with the minimum size of building footprints in the considered scene. $\mathbf{X}_{\text{LR}}^3$ was thresholded according to the unsupervised split-based procedure described in section III-A. The split size was calculated starting from the average building size, which was estimated to be $w_1 \times w_2 \times h = 25 \times 20 \times 15$ m^3. By substituting these values in eq. (2) S_{SR} was obtained to be equal to 49.50 m in slant-range geometry. Since the CSK images are ground-projected, S_{SR} was projected in ground range considering the reference incidence angle i.e., 58 degree obtaining in this way $S_{GR} = 58.36$ m. From the calculation and taking into account a pixel spacing in range of 0.5 m, S_R results to be equal to 120 pixels. By applying eq. (3) and considering a pixel spacing in azimuth of 0.5 m, S_A was estimated to be equal to 40 pixels. It is worth noting that the split-based thresholding technique has a relative high tolerance to the selection of the values of S_R and S_A. This was proven by a sensitivity analysis in which S_A was ranged from 20 to 60 pixels and S_R from 80 to 170 pixels. Despite the large range (about $\pm 1/3$ of the optimal selected size) the error on the estimation of the thresholds is small. That is of 0.054 in average with a peak value of 0.14 for $\hat{t}^-$, and of 0.045 in average with a peak value of 0.15 for $\hat{t}^+$. Moreover, in all the cases the generated maps did not present any critical behavior and resulted in a very similar final detection of changed buildings. The obtained CD map $\mathbf{M}^{\text{opt}}$ highlighting the three classes ξ_u, ξ^+, ξ^- is reported in Fig. 11c. The detector described by (5) was then applied to $\mathbf{M}^{\text{opt}}$ in order to obtain the image $\mathbf{C}$. With regard to the considered scene, it is expected that the minimum size of building footprint is 40×20 pixels. Therefore, the set of 5 windows reported in Fig. 7 were set to size $z_1 \times z_2 = 40 \times 20$ pixels in order to derive $\mathbf{C}$ (see Fig. 11d). A set of changed areas $\Gamma = \{\gamma_1, \ldots, \gamma_{49}\}$ compatible with building footprint changes was derived by threhsolding $\mathbf{C}$ with $T_C = 160$ (which corresponds to 20% of maximum value of $\mathbf{C}$) and by applying a flood-fill algorithm. It is worth noting that both the window size and the threshold value were selected according to minimum size of buildings in the considered area in order to limit the missed alarms. Each of the candidate areas was analyzed in order to detect the changed buildings. To this end the four fuzzy rules were automatically evaluated for each candidate γ_h, $(h = 1, \ldots, 49)$. Finally, for each building candidate that presents an aggregated membership $T_{\mathbf{M}}$ greater than 0.125 the radar building footprint was approximated by the convex-hull containing the candidate. It is worth noting that $T_{\mathbf{M}}$ was selected in order to minimize the missed alarms. This is done by taking into account the definition of the membership functions and the aggregation strategy (i.e., algebraic product). In the present experiment $\mu_{rs} = \mu_{rl} = \mu_\alpha = 0.5$ were selected as limit case, which results in an aggregate membership function $\text{M} = 0.125$. Fig. 11e shows the final result. In the specific case, all the reconstructed radar building footprints have an aggregate membership function greater than 0.615. Table IVa reports the settings of the parameters used for the dataset of L'Aquila.

By comparing the changed building map with the false color composition of the multitemporal images (Fig. 11e)

(a)


Increase of backscattering
Decrease of backscatteing
Unchanged

(b)

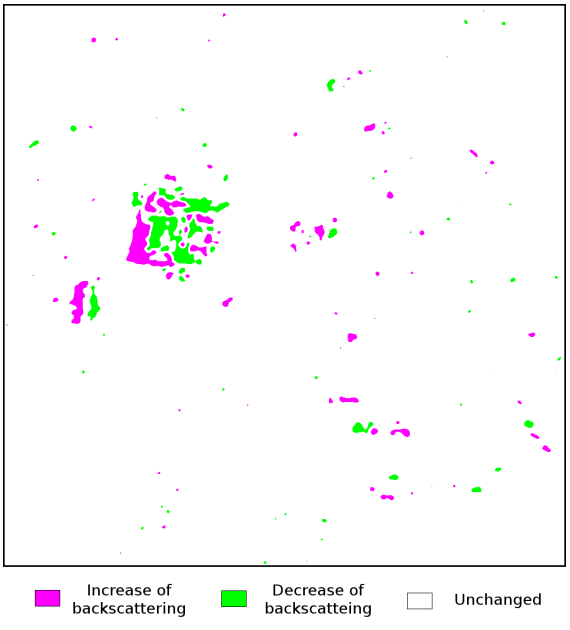
Increase of backscattering
Decrease of backscatteing
Unchanged

(c)

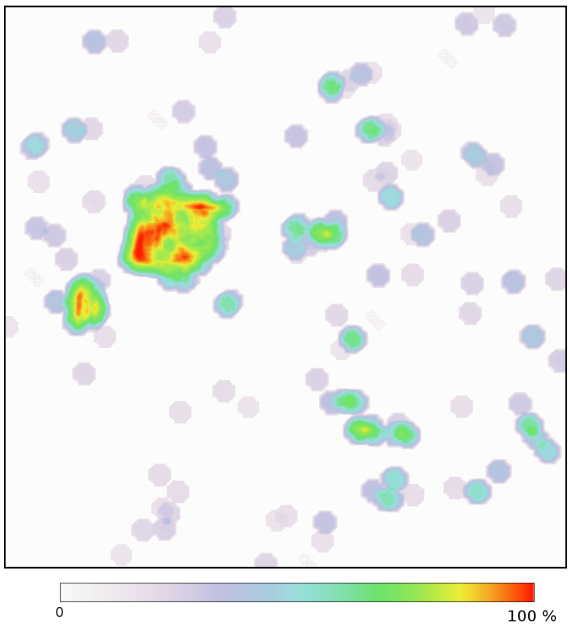
0
100 %

(d)

(e)

Fig. 13: Trento (Italy) data set: (a) optical image (2011 [36]); and (b) RGB multitemporal composition of spotlight TerraSAR-X and TanDEM-X images (R:03/04/2013, G:21/01/2011, B:03/04/2013). (c) Change detection map $\mathbf{M}^{\mathrm{opt}}$ obtained at the level $N-1=3$. (d) Map showing the index of the size of changes $\mathbf{C}$. (e) Changed building map overlapped to the RGB multitemporal composition of CSK data.

one can notice that the proposed approach can effectively detect the backscattering changes associated to disappeared buildings as described in Section II-B, which patterns present a decrease and increase of backscattering oriented near-to-far-range (see Fig. 11e). From a quantitative point of view, Table II reports the number of total buildings present in the scene and the total number of demolished radar building footprints correctly detected and missed by the proposed approach. Even though the dataset presents a relevant number of changes in the backscattering value, none of the actual demolished buildings (see Figg. 12a-d) was miss-detected and only one building was wrongly identified as destroyed (see Fig. 12.e). As a matter of fact, from the orthophotos and the optical images [36] acquired after the CSK acquisition of September 2009, it was observed that this building was seriously damaged from the earthquake and demolished by the authorities after the acquisition. Fig. 11f shows the position of the destroyed buildings in the cadestrial map obtained by transforming the geometry of SAR images to the geo-referenced cadastral map. The analysis confirms the high accuracy of the proposed technique. It is worth noting that the detected demolished buildings has different aspect angle ϕ. Moreover, even though the density of buildings in the considered site is high, the proposed approach can effectively discriminate between demolished and standing buildings. This points out the high robustness of the proposed technique to the possible deviations from the adopted ideal model of changes. A similar analysis has been performed for changes that are not associated with buildings, i.e., ω_{c3} (yellow areas

in Fig. 11d). The orthophotos point out that these changes are not associated to fully destroyed buildings, but to the post earthquake activities e.g., emergency housing units or to partially damaged buildings. This confirms the effectiveness of the proposed method also in the detection of general changes.

B. Trento Data Set: Detection of New Buildings

The second data set is made up of two high resolution spotlight single look slant range complex images acquired by TerraSAR-X and TanDEM-X with resolution 0.58 m in range by 1.1 m in azimuth (0.454 by 0.855 meters of pixel spacing) in X-band HH-polarization. The images have been taken on January 21, 2011 and April 3, 2013 over the city of Trento ($46°04'$N $11°07'$E), with a perpendicular baseline of 489.29 m in ascending orbit with $53°$ incidence angle. The selected test site is a section (1024×1024 pixels) of the full scene where the department of engineering and computer science of the University of Trento and the Fondazione Bruno Kessler (FBK) are represented. Fig. 13a shows the optical image corresponding to the same area [36]. Fig. 13b shows a false color composition of the two images (R:03/04/2013, G:21/01/2011, B:03/04/2013) in which pixels with an increase in the value of backscattering appear in magenta tone, pixels with a decrease in the value of backscattering appear in green tone and unchanged pixel in gray-scale. From a ground field survey it is know that three new buildings were built up in the considered site. Moreover, several buildings were subject to restoration works. As one can notice, in this data-set the size of the changed buildings is not homogeneous: we have a large building (still partially under construction during the second acquisition) in the center left of the image, a medium size building in the left part of the image and a small building in the center of the image. Therefore, we aim to test the robustness of the proposed approach to this heterogeneous condition.

In order to apply the proposed method the two VHR SAR images were calibrated (radar brightness) and coregistered (with sub-pixel accuracy) and the log-ratio image $\mathbf{X}_{\mathrm{LR}}$ calculated. In the considered city, it is expected that the smallest radar footprint of a building is about 20 by 10 meters. Considering the proposed multiscale approach the resolution of $\mathbf{X}_{\mathrm{LR}}^{\mathrm{opt}}$ is approximately given by $1.1 \cdot 2^{(N-1)}$ in the worst case i.e., in azimuth. Therefore the level $(N-1)^{\mathrm{th}} = 3^{\mathrm{rd}}$, which gives a resolution of 8.8 m is suitable for the purpose. The automatic split-based thresholding approach was applied to $\mathbf{X}_{\mathrm{LR}}^{3}$ in order to derived $\mathbf{M}^{\mathrm{opt}}$. The split size was calculated starting from the average building size, which was estimated to be $w_1 \times w_2 \times h = 30 \times 80 \times 13$ m^3. By substituting these values in eq. (2) S_R was obtained to be equal to 45.56 m in slant-range geometry. By taking into account the pixel spacing in range of 0.454 m S_R results to be equal to about 100 pixels. By applying eq. (3) and considering a pixel spacing in azimuth of 0.855 m, S_A was estimated to be equal to about 90 pixels. Fig. 13c shows the CD map $\mathbf{M}^{\mathrm{opt}}$ generated with the split-based thresholding method from $\mathbf{X}_{\mathrm{LR}}^{3}$. As done for the dataset of L'Aquila a sensitivity analysis was performed. By ranging S_R and S_A from 60 to 120 the error on the estimation of the thresholds is small. That is of 0.058 in average with a peak of 0.14 for $\hat{t}^{-}$, and of 0.041 in average with a peak of 0.1 for $\hat{t}^{+}$. In all the cases the generated maps did not present any critical behavior and resulted in a very similar final detection of changed buildings. The index image $\mathbf{C}$ (Fig. 13d) was derived by applying the set of filters described by (5) to $\mathbf{M}^{\mathrm{opt}}$ with size $z_1 \times z_2 = 20 \times 10$ pixels selected according to the expected minimum radar building footprint size. $\mathbf{C}$ was

TABLE III: Performance of the proposed approach for Trento Dataset in terms of number of detected new buildings and missed new buildings. The total number of buildings present in the site is also reported in the table.

Total Number of Buildings	Number of New Buildings (reference)	Detected New Buildings (ω_{c2})	Missed New Buildings
187	3	3	0

Fig. 14: New large building in the Trento dataset: some month before the 2011 TerraSAR-X acquisition (on the left) and on the same day of the second acquisition (on the right). As one can notice the building is still under construction during the second acquisition with several materials and vehicles present in the building site.

thresholded and 25 candidates were detected. They were analyzed in order to discriminate the appropriate class of change by testing the proposed fuzzy rules. Table IVb reports the settings of the parameters used for the dataset of Trento.

As one can observe from the changed building map (Fig. 13e) the proposed approach allows the detection of

TABLE IV: Parameters used in the experiments carried out on: a) L'Aquila dataset; and b) Trento dataset.

Parameter	Value
$N-1$	3
S_R	120 pixels
S_A	40 pixels
z_1	40 pixels
z_2	20 pixels
T_C	160 pixels
a_1, b_1	10, 0.3
a_2, b_2	10, 0.5
a_3, b_3	-10, $\frac{\pi}{3}$
T_{M}	> 0.125

(a)

Parameter	Value
$N-1$	3
S_R	100 pixels
S_A	90 pixels
z_1	20 pixels
z_2	10 pixels
T_C	40 pixels
a_1, b_1	10, 0.3
a_2, b_2	10, 0.5
a_3, b_3	-10, $\frac{\pi}{3}$
T_{M}	> 0.125

(b)

the building footprint of the three new buildings. The aggregated membership values for all buildings is always grater than 0.74. In detail, for the small and the medium size buildings the reconstructed building footprints result to be accurate. The footprint for the large building in the center left of the image was reconstructed considering the several regions of increase and decrease in backscattering that arise because of both the complexity of the structure of the building (i.e., a inner court and three front wings) and the construction works, which were still in progress during the second TerraSAR-X acquisition (see Fig. 14a). As consequence the reconstructed footprint results to be divided in different parts. Nevertheless, the building footprint is completely detected even if in this case we are far from the ideal reference condition of the considered model.

Table III reports the total number of buildings present in the scene and the number of new buildings detected and missed by the proposed approach. Even though the size of the new buildings present in the scene is not homogeneous, none of the actual new buildings were missed from the detection and only one building was wrongly identified as destroyed with a relatively low membership of 0.39. As a matter of fact, from the ground field survey it is known that this building was completely renovated between the two acquisitions. Thus the building footprint really changed in the considered time interval. As for L'Aquila dataset, the proposed approach can effectively discriminate between demolished and standing buildings despite the high density of buildings in the area. A further analysis has been performed on changes that are not associated to fully destroyed or new buildings to buildings i.e., ω_{c3} (yellow areas in Fig. 13e), which result to be buildings partially renovated. This confirms the effectiveness of the proposed method in the detection of changes in buildings.

V. Conclusion

In this paper an approach to building CD in multitemporal VHR SAR images has been proposed that detects changes by distinguishing between new and demolished buildings. The approach is based on two concepts: i) the extraction of information on changes associated with increase and decrease of backscattering at the optimal building scale; and ii) the exploitation of the expected backscattering properties of buildings to detect either new and fully demolished buildings with their grade of reliability.

The method takes advantage of the theoretical modeling of the backscattering mechanisms in multitemporal VHR SAR images. From this modeling new and destroyed buildings can be identified by a pattern made up of an area of both increase and decrease of backscattering with specific spatial properties and a specific alignment. In order to extract the changes associated with increase and decrease of backscattering, the proposed approach makes use of a multiscale representation of the multitemporal information. This allows a detection of changes at the optimal building scale. This means that the changes smaller than the selected building scale are rejected while the changes related to building size are made homogeneous. This information is used to identify the candidates to be changed buildings. The building candidates are analyzed in order to properly detect the new or destroyed building by means of four fuzzy rules. The fuzzy rules are formulated by taking into account the ideal backscattering mechanisms that arise when a building appears or disappears between two acquisitions. The aggregated membership resulting from the application of the fuzzy rules makes it possible to identify the class of each building candidate (i.e.,

new/destroyed building or general change with size comparable to the building size but not related to new or destroyed building). Moreover, the membership value gives an indication of the reliability of the detected class. The proposed approach requires the tuning of some parameters that depend on the approximated size of the buildings in the investigated area. This is a prior information usually available and easy to include in the processing. It is worth remarking that after this tuning the method is completely automatic.

The proposed approach was tested on two VHR SAR dataset acquired by two different X-band systems i.e., COSMOSky-Med and TerraSAR-X/Tandem-X. The first dataset is related to the earthquake of L'Aquila (Italy) in 2009. Here the changes are mainly associated to demolished buildings. The second data set is related to a condition of urban expansion with the construction of new buildings in the city of Trento (Italy). In both cases the proposed method demonstrated to be effective in detecting both new and demolished buildings with a high accuracy. In detail, only two buildings were misclassified over 387 present in the two datasets with no missed detection. This was possible also because of the high robustness of the proposed method to deviations from the ideal model considered for changes. This robustness is due to both the use of adequate fuzzy rules and the intrinsic reliability obtained when working on the comparison of two images rather than on the modeling of building on each image.

As future development of this work, we plan to improve the building detector by better modeling the geometrical behaviors of building primitives. Moreover, we plan to investigate the possibility to discriminate among several building construction stages and/or building damage levels.

APPENDIX

NOTATION USED IN THE PAPER

The mathematical notation used in the paper is listed in the following. Symbols are listed in the appearance order.

$w_1 \times w_2 \times h$	Building dimensions.
ϕ	Aspect angle.
θ	Incidence angle.
w_b	Building width limit.
$\mathbf{X}_\tau$	VHR SAR images acquired at time τ.
ω_u	Class of unchanged pixels.
ω_{c1}	Class of fully destroyed buildings.
ω_{c2}	Class of new buildings.
ω_{c3}	Class of changes that have size comparable to a building but do not present the typical pattern of full new/demolished buildings.
ω_{c4}	Class of changes that do not show a size comparable to a building.
$\mathbf{X}_{\mathrm{LR}}$	Log-ratio image.
$\mathbf{X}_{\mathrm{LR}}^n$	Multiscale representation of the log-ratio information at the n-th level.

$N-1$	Optimal building level.
$\mathbf{M}^{\mathrm{opt}}$	Map of changes at the optimal scale.
ξ_u	Class of unchanged pixels.
ξ^+	Class of increase of backscattering.
ξ^-	Class of decrease of backscattering.
$\hat{t}^+, \hat{t}^-$	Estimated thresholds for the discrimination of ξ_u, ξ^+ and ξ^-.
S_A	Split length along azimuth.
S_R	Split length along range.
Γ	Set of changed building candidates.
Δ	Set of regions of change that made up a building candidate.
$z_1 \times z_2$	Window size for the search of candidates.
$\mathbf{C}$	Index of the size of change.
T_c	Threshold for extracting the candidate regions Γ from the index image $\mathbf{C}$.
μ_p	Membership function to test the degree of completeness.
μ_{r_s}	Membership function to test the degree of the proportionality of the areas.
μ_{r_l}	Membership function to test the degree of the equivalence of the lengths.
$\mu_{\lvert\alpha\rvert}$	Membership function to test the degree of the alignment.
a_1, a_2, a_3	Parameters for tuning the slope of the sigmoid.
b_1, b_2, b_3	Parameters for tuning the center of the sigmoid.
T_M	Threshold on the aggregate membership.

ACKNOWLEDGMENT

The authors would like to thank the Italian Space Agency (ASI) for providing the CSK images of L'Aquila within the agreement no. I/041/09/0, project ID-2181. The authors would also like to thank the German Aerospace Center (DLR) for providing the TerraSAR-X images of Trento which were acquired in the framework of the ISPRS WG VII/2 and TerraSAR Project LAN0634.

REFERENCES

[1] P. Gamba, "Human settlements: A global challenge for EO data processing and interpretation," *Proceedings of the IEEE*, vol. 101, no. 3, pp. 570–581, 2013.

[2] F. Henderson and Z.-G. Xia, "SAR applications in human settlement detection, population estimation and urban land use pattern analysis: a status report," *IEEE Trans. Geosci. Remote Sens.*, vol. 35, no. 1, pp. 79–85, 1997.

[3] P. Du, S. Liu, P. Gamba, K. Tan, and J. Xia, "Fusion of difference images for change detection over urban areas," *IEEE J. Sel. Topics Appl. Earth Observations Remote Sens.*, vol. 5, no. 4, pp. 1076–1086, 2012.

[4] T. Balz, "SAR simulation of urban areas: Techniques and applications," in *Radar Remote Sensing of Urban Areas*, ser. Remote Sensing and Digital Image Processing, U. Soergel, Ed. Springer Netherlands, 2010, vol. 15, pp. 215–231.

[5] R. Dekker, "Texture analysis and classification of ERS SAR images for map updating of urban areas in The Netherlands," *IEEE Trans. Geosci. Remote Sens.*, vol. 41, no. 9, pp. 1950–1958, 2003.

[6] U. Soergel, U. Thoennessen, A. Brenner, and U. Stilla, "High-resolution sar data: new opportunities and challenges for the analysis of urban areas," *Radar, Sonar and Navigation, IEE Proceedings* -, vol. 153, no. 3, pp. 294–300, 2006.

[7] A. Brenner and L. Roessing, "Radar imaging of urban areas by means of very high-resolution sar and interferometric sar," *IEEE Trans. Geosci. Remote Sens.*, vol. 46, no. 10, pp. 2971–2982, 2008.

[8] Y. Dong, B. Forster, and C. Ticehurst, "Radar backscatter analysis for urban environments," *International Journal of Remote Sensing*, vol. 18, no. 6, pp. 1351–1364, 1997.

[9] G. Franceschetti, A. Iodice, and D. Riccio, "A canonical problem in electromagnetic backscattering from buildings," *IEEE Trans. Geosci. Remote Sens.*, vol. 40, no. 8, pp. 1787 – 1801, aug 2002.

[10] Z.-G. Xia and F. Henderson, "Understanding the relationships between radar response patterns and the bio- and geophysical parameters of urban areas," *IEEE Trans. Geosci. Remote Sens.*, vol. 35, no. 1, pp. 93–101, 1997.

[11] L. Bruzzone and F. Bovolo, "A novel framework for the design of change-detection systems for very-high-resolution remote sensing images," *Proceedings of the IEEE*, vol. 101, no. 3, pp. 609–630, 2013.

[12] F. Bovolo, C. Marin, and L. Bruzzone, "A hierarchical approach to change detection in very high resolution SAR images for surveillance applications," *IEEE Trans. Geosci. Remote Sens.*, vol. 51, no. 4, pp. 2042–2054, 2013.

[13] M. Matsuoka and F. Yamazaki, "Use of satellite SAR intensity imagery for detecting building areas damaged due to earthquakes," *Earthquake Spectra*, vol. 20, pp. 975–994, 2004.

[14] M. Chini, N. Pierdicca, and W. Emery, "Exploiting SAR and VHR optical images to quantify damage caused by the 2003 Bam earthquake," *IEEE Trans. Geosci. Remote Sens.*, vol. 47, no. 1, pp. 145–152, 2009.

[15] D. Ehrlich, H. Guo, K. Molch, J. Ma, and M. Pesaresi, "Identifying damage caused by the 2008 Wenchuan earthquake from VHR remote sensing data," *International Journal of Digital Earth*, vol. 2, no. 4, pp. 309–326, 2009.

[16] D. Brunner, G. Lemoine, and L. Bruzzone, "Earthquake damage assessment of buildings using VHR optical and SAR imagery," *IEEE Trans. Geosci. Remote Sens.*, vol. 48, no. 5, pp. 2403 –2420, may 2010.

[17] T. Balz and M. Liao, "Building-damage detection using post-seismic high-resolution SAR satellite data," *International Journal of Remote Sensing*, vol. 31, no. 13, pp. 3369–3391, 2010.

[18] R. Dekker, "High-resolution radar damage assessment after the earthquake in Haiti on 12 january 2010," *IEEE J. Sel. Topics Appl. Earth Observations Remote Sens.*, vol. 4, no. 4, pp. 960 –970, dec. 2011.

[19] F. Dell'Acqua, C. Bignami, M. Chini, G. Lisini, D. Polli, and S. Stramondo, "Earthquake damages rapid mapping by satellite remote sensing data: L'Aquila april 6th, 2009 event," *IEEE J. Sel. Topics Appl. Earth Observations Remote Sens.*, vol. 4, no. 4, pp. 935 –943, dec. 2011.

[20] Y. Dong, Q. Li, A. Dou, and X. Wang, "Extracting damages caused by the 2008 Ms 8.0 Wenchuan earthquake from SAR remote sensing data," *Journal of Asian Earth Sciences*, vol. 40, no. 4, pp. 907 – 914, 2011, the 2008 Wenchuan Earthquake, China and Active Tectonics of Asia.

[21] D. Jin, X. Wang, A. Dou, and Y. Dong, "Post-earthquake building damage assessment in Yushu using airborne SAR imagery," *Earthquake Science*, vol. 24, no. 5, pp. 463–473, 2011.

[22] L. Dong and J. Shan, "A comprehensive review of earthquake-induced building damage detection with remote sensing techniques," *ISPRS Journal of Photogrammetry and Remote Sensing*, vol. 84, no. 0, pp. 85 – 99, 2013.

[23] V. Poulain, J. Inglada, M. Spigai, J.-Y. Tourneret, and P. Marthon, "High-resolution optical and SAR image fusion for building database updating," *IEEE Trans. Geosci. Remote Sens.*, vol. 49, no. 8, pp. 2900–2910, 2011.

[24] J. Tao, S. Auer, and P. Reinartz, "Detecting changes between a dsm and a high resolution sar image with the support of simulation based separation of urban scenes," in *Synthetic Aperture Radar, 2012. EUSAR. 9th European Conference on*, 2012, pp. 95–98.

[25] P. Brett and R. Guida, "Earthquake damage detection in urban areas using curvilinear features," *IEEE Trans. Geosci. Remote Sens.*, vol. 51, no. 9, pp. 4877–4884, 2013.

[26] A. Ferro, D. Brunner, L. Bruzzone, and G. Lemoine, "On the relationship between double bounce and the orientation of buildings in VHR SAR images," *IEEE Geosci. Remote Sens. Lett.*, vol. 8, no. 4, pp. 612 –616, july 2011.

[27] F. Bovolo, C. Marin, and L. Bruzzone, "A novel approach to building change detection in very high resolution SAR images," in *Proc. SPIE*, vol. 8537, 2012, pp. 85 370Y–85 370Y–12.

[28] C. Marin, F. Bovolo, and L. Bruzzone, "Detection of changed buildings in multitemporal very high resolution SAR images," in *Geoscience and Remote Sensing Symposium (IGARSS), 2013 IEEE International*, July 2013, pp. 3443–3446.

[29] U. Soergel, U. Thönnessen, and U. Stilla, "Iterative building reconstruction from multi-aspect insar data," in *3-D reconstruction from airborne laserscanner and InSAR data. International Archives of Photogrammetry and Remote Sensing.*, Maas, Vosselmann, and Streilein, Eds., vol. 34, 2003, pp. 186–192.

[30] M. Quartulli and M. Datcu, "Stochastic geometrical modeling for built-up area understanding from a single SAR intensity image with meter resolution," *IEEE Trans. Geosci. Remote Sens.*, vol. 42, no. 9, pp. 1996–2003, 2004.

[31] A. Thiele, E. Cadario, K. Schulz, U. Thonnessen, and U. Soergel, "Building recognition from multi-aspect high-resolution InSAR data in urban areas," *IEEE Trans. Geosci. Remote Sens.*, vol. 45, no. 11, pp. 3583–3593, 2007.

[32] F. Xu and Y.-Q. Jin, "Automatic reconstruction of building objects from multiaspect meter-resolution sar images," *IEEE Trans. Geosci. Remote Sens.*, vol. 45, no. 7, pp. 2336–2353, 2007.

[33] R. Guida, A. Iodice, D. Riccio, and U. Stilla, "Model-based interpretation of high-resolution sar images of buildings," *Selected Topics in Applied Earth Observations and Remote Sensing, IEEE Journal of*, vol. 1, no. 2, pp. 107–119, 2008.

[34] H. Sportouche, F. Tupin, and L. Denise, "Extraction and three-dimensional reconstruction of isolated buildings in urban scenes from high-resolution optical and SAR spaceborne images," *IEEE Trans. Geosci. Remote Sens.*, vol. 49, no. 10, pp. 3932–3946, 2011.

[35] A. Ferro, D. Brunner, and L. Bruzzone, "Automatic detection and reconstruction of building radar footprints from single VHR SAR images," *IEEE Trans. Geosci. Remote Sens.*, vol. 51, no. 2, pp. 935–952, 2013.

[36] "Google maps." [Online]. Available: https://maps.google.com

[37] C. Oliver and S. Quegan, *Understanding Synthetic Aperture Radar Images*, ser. SciTech radar and defense series. SciTech Publ., 2004.

[38] A. Bennett and D. Blacknell, "Infrastructure analysis from high resolution SAR and InSAR imagery," in *Remote Sensing and Data Fusion over Urban Areas, 2003. 2nd GRSS/ISPRS Joint Workshop on*, may 2003, pp. 230 – 235.

[39] Y. Zhang, H. Chen, C. Ding, and H. Wang, "A novel approach for shadow enhancement in high-resolution SAR images using the height-variant phase compensation algorithm," *IEEE Geosci. Remote Sens. Lett.*, vol. 10, no. 1, pp. 189–193, 2013.

[40] J. Groen, R. Hansen, H. Callow, J. Sabel, and T. Sabo, "Shadow enhancement in synthetic aperture sonar using fixed focusing," *Oceanic Engineering, IEEE Journal of*, vol. 34, no. 3, pp. 269–284, 2009.

[41] P. Burt and E. Adelson, "The laplacian pyramid as a compact image code," *Communications, IEEE Transactions on*, vol. 31, no. 4, pp. 532–540, 1983.

[42] S. Mallat, "A theory for multiresolution signal decomposition: the wavelet representation," *Pattern Analysis and Machine Intelligence, IEEE Transactions on*, vol. 11, no. 7, pp. 674–693, 1989.

[43] G. Nason and B. Silverman, "The stationary wavelet transform and some statistical applications," in *Wavelets and Statistics*, ser. Lecture Notes in Statistics, A. Antoniadis and G. Oppenheim, Eds. Springer New York, 1995, vol. 103, pp. 281–299.

[44] F. Bovolo and L. Bruzzone, "A detail-preserving scale-driven approach to change detection in multitemporal SAR images," *IEEE Trans. Geosci. Remote Sens.*, vol. 43, no. 12, pp. 2963 – 2972, dec. 2005.

[45] Y. Bazi, L. Bruzzone, and F. Melgani, "An unsupervised approach based on the generalized Gaussian model to automatic change detection in multitemporal SAR images," *IEEE Trans. Geosci. Remote Sens.*, vol. 43, no. 4, pp. 874 – 887, april 2005.

[46] E. Rignot and J. van Zyl, "Change detection techniques for ERS-1 SAR data," *IEEE Trans. Geosci. Remote Sens.*, vol. 31, no. 4, pp. 896 –906, jul 1993.

[47] F. Bovolo and L. Bruzzone, "A split-based approach to unsupervised change detection in large-size multitemporal images: Application to tsunami-damage assessment," *IEEE Trans. Geosci. Remote Sens.*, vol. 45, no. 6, pp. 1658 –1670, june 2007.

[48] Y. Bazi, L. Bruzzone, and F. Melgani, "Image thresholding based on the EM algorithm and the generalized Gaussian distribution," *Pattern Recogn.*, vol. 40, no. 2, pp. 619–634, Feb. 2007.

[49] A. P. Dempster, N. M. Laird, and D. B. Rubin, "Maximum likelihood from incomplete data via the EM algorithm," *Journal of the Royal Statistical Society, Series B*, vol. 39, no. 1, pp. 1–38, 1977.

[50] L. Zadeh, "Fuzzy sets," *Information and Control*, vol. 8, no. 3, pp. 338 – 353, 1965.

[51] P. Heckbert, *Graphics Gems IV*, ser. Graphics gems series. AP Professional, 1994.

[52] P. M. Larsen, "Industrial applications of fuzzy logic control," *International Journal of Man-Machine Studies*, vol. 12, no. 1, pp. 3 – 10, 1980.

[53] C. B. Barber, D. P. Dobkin, and H. Huhdanpaa, "The quickhull algorithm for convex hulls," *ACM Trans. Math. Softw.*, vol. 22, no. 4, pp. 469–483, Dec. 1996.

[54] D. Brunner, K. Schulz, and T. Brehm, "Building damage assessment in decimeter resolution sar imagery: A future perspective," in *Urban Remote Sensing Event (JURSE), 2011 Joint*, 2011, pp. 217–220.

[55] S. Kuny, K. Schulz, and H. Hammer, "Signature analysis of destroyed buildings in simulated high resolution SAR data," in *Geoscience and Remote Sensing Symposium (IGARSS), 2013 IEEE International*, 2013.

[56] "Geoportale regione abruzzo." [Online]. Available: http://geoportale.regione.abruzzo.it/

[57] "Bing maps." [Online]. Available: www.bing.com/maps/